A complete version
Preprint typeset using LaTeX style emulateapj v. 08/22/09

MULTI-SIGHTLINE OBSERVATION OF NARROW ABSORPTION LINES IN LENSED QUASAR SDSS J1029+2623[1,2]

Toru Misawa[3], Cristian Saez[4,5], Jane C. Charlton[6], Michael Eracleous[6,7], George Chartas[8], Franz E. Bauer[9,10,11], Naohisa Inada[12], and Hisakazu Uchiyama[13]

A complete version

ABSTRACT

We exploit the widely-separated images of the lensed quasar SDSS J1029+2623 ($z_{\rm em}$=2.197, θ = 22.″5) to observe its outflowing wind through two different sightlines. We present an analysis of three observations, including two with the Subaru telescope in 2010 February (Misawa et al. 2013) and 2014 April (Misawa et al. 2014b), separated by 4 years, and one with the Very Large Telescope, separated from the second Subaru observation by ∼2 months. We detect 66 narrow absorption lines (NALs), of which 24 are classified as *intrinsic* NALs that are physically associated with the quasar based on partial coverage analysis. The velocities of intrinsic NALs appear to cluster around values of $v_{\rm ej}$ ∼ 59,000, 43,000, and 29,000 km s^{-1}, which is reminiscent of filamentary structures obtained by numerical simulations. There are no common intrinsic NALs at the same redshift along the two sightlines, implying that the transverse size of the NAL absorbers should be smaller than the sightline distance between two lensed images. In addition to the NALs with large ejection velocities of $v_{\rm ej}$ > 1,000 km s^{-1}, we also detect broader proximity absorption lines (PALs) at $z_{\rm abs} \sim z_{\rm em}$. The PALs are likely to arise in outflowing gas at a distance of $r \leq 620$ pc from the central black hole with an electron density of $n_{\rm e} \geq 8.7{\times}10^3$ cm^{-3}. These limits are based on the assumption that the variability of the lines is due to recombination. We discuss the implications of these results on the three-dimensional structure of the outflow.

Subject headings: quasars: absorption lines – quasars: individual (SDSS J1029+2623)

1. INTRODUCTION

AGN outflows, potentially powered by one or more of a variety of mechanisms (e.g., radiation force, magnetic pressure, and magnetocentrifugal force), are important ingredients of quasar central engines and likely play a role in quasar and galaxy formation/evolution because: 1) they extract angular momentum from accretion disks allowing gas accretion to proceed (e.g., Blandford & Payne 1982; Emmering, Blandford, and Shlosman 1992; Konigl & Kartje 1994; Everett 2005), leading to the growth of black holes, 2) they also provide energy and momentum feedback to the interstellar medium of host galaxies and to the intergalactic medium (IGM), and inhibit star formation (e.g., Springel, Di Matteo, & Hernquist 2005), and 3) they may promote metal enrichment of the intergalactic medium (IGM) (e.g., Hamann et al. 1997b; Gabel, Arav, & Kim 2006). These outflowing gases, which are difficult to observe directly, have been detected as absorption lines in the spectra of about 50% of all quasars (e.g., Vestergaard 2003; Wise et al. 2004; Misawa et al. 2007a; Nestor et al. 2008; Muzahid et al. 2013). However, a limitation of these past studies is that they observe the outflowing gas *only* along a single sightline (i.e., one dimension) toward the nucleus of each quasar, although the absorber's physical conditions probably depend on the location/orientation at which we observe it (e.g., Ganguly et al. 2001; Elvis 2000). Thus, the internal structure of outflowing winds is still largely unknown.

Multiple quasar images, produced by gravitational lensing, provide a unique way to study the outflowing gas along more than one sightline. Lensed quasars with large image separation angles have a higher chance of revealing structural differences in the outflowing winds, especially in the vicinity of the continuum source. In this sense, the quasar images that are lensed by a cluster of galaxies (rather than a single massive galaxy) are very promising targets. Among three such lensed quasars, SDSS J1029+2623 at z_{em} ∼2.197 (Inada et al. 2006; Oguri et al. 2008) is the best target because i) it has the largest lensed quasar image separation ($\theta \sim 22.''5$) ever observed (see Figure 1 of Inada et al. 2006), and ii) it exhibits absorption features in the blue wings of the C IV, N V, and Lyα emission lines with ejection velocity of $v_{\rm ej} \leq$

Electronic address: misawatr@shinshu-u.ac.jp
[1] Based on data collected at Subaru Telescope, which is operated by the National Astronomical Observatory of Japan.
[2] Based on observations obtained at the European Southern Observatory at La Silla, Chile in programs 092.B-0512(A)
[3] School of General Education, Shinshu University, 3-1-1 Asahi, Matsumoto, Nagano 390-8621, Japan
[4] Korea Astronomy and Space Science Institute (KASI), 61-1, Hwaam-dong, Yuseong-gu, Deajeon 305-348, Republic of Korea
[5] Department of Astronomy, University of Maryland, College Park, MD 20742-2421
[6] Department of Astronomy and Astrophysics, Pennsylvania State University, University Park, PA 16802
[7] Department of Astronomy & Astrophysics and Center for Gravitational Wave Physics, The Pennsylvania State University, 525 Davey Lab, University Park, PA 16802
[8] Department of Physics and Astronomy, College of Charleston, SC 29424
[9] Instituto de Astrofísica, Facultad de Física, Pontificia Universidad Católica de Chile, Casilla 306, Santiago 22, Chile
[10] Millennium Institute of Astrophysics (MAS), Nuncio Monseñor Sótero Sanz 100, Providencia, Santiago, Chile
[11] Space Science Institute, 4750 Walnut Street, Suite 205, Boulder, Colorado 80301
[12] Department of Physics, National Institute of Technology, Nara College, Yamatokohriyama, Nara 639-1080, Japan
[13] Department of Astronomy, School of Science, Graduate University for Advanced Studies, Mitaka, Tokyo 181-8588, Japan

1,000 km s^{-1}, which could be the result of outflowing gas moving toward us from the central region. We call them Proximity Absorption Lines (PALs) throughout this paper. We define PALs as a subcategory of Narrow Absorption Lines (NALs) with ejection velocity of $v_{\rm ej} \leq$ 1,000 km s^{-1}. We use this terminology throughout the paper to separate PALs from NALs with larger ejection velocities.

Misawa et al. (2013) obtained high-resolution spectra of the brighter two of the lensed images (images A and B) with the Subaru telescope in 2010 February and found several clear signs that the origin of the PALs is indeed in the outflowing gas. First, they show the signature of partial coverage, which means the absorbers do not cover the background flux source completely. There also exists a clear difference in the absorption profiles between the spectra of images A and B, which can be explained by either of the following two scenarios: (a) time variability of the absorption features over a time scale corresponding to the time delay between the two images (*time variation scenario*; Chartas et al. 2007)[14], or (b) a difference in the absorption between the different sightlines of the outflowing wind (*multi-sightline scenario*; Chelouche 2003; Green 2006). However, with a single-epoch observation we cannot distinguish between these scenarios. Misawa et al. (2014b) performed a second observation about four years (1514 days in the observed frame) after the first observation (which is longer than the time delay between images A and B, $\Delta t_{\rm AB} \sim 744$ days), and found that the PALs were nearly stable and that most of the differences between images A and B still remained. This evidence suggests a *multi-sightline scenario* where the absorber's size should be smaller than the physical distance between the sightlines of the lensed images, thus not covering both sightlines. A possible explanation is that there are a number of small *clumpy* clouds in the outflowing stream. Indeed, some of the outflowing gas is expected to consist of small gas clouds ($d_{\rm cloud} \leq 10^{-3}$ pc) with very large gas densities ($n_e \geq 10^6$ cm^{-3}; Hamann et al. 2013; Joshi et al. 2014). Furthermore, recent radiation-MHD simulations by Takeuchi et al. (2013) reproduce variable clumpy structures with typical sizes of 20 times the gravitational radius ($R_{\rm g}$), corresponding to $d_{\rm cloud} \sim 5{\times}10^{-4}$ pc, assuming a black-hole mass for SDSS J1029+2623 of $M_{\rm BH} \sim 10^{8.72}$ M$_\odot$ (Misawa et al. 2013).

Such clumpy clouds can be examined more easily through narrow absorption lines (NALs, hereafter) with large offset velocities from the quasar because the corresponding absorbers are (i) probably smaller than the PAL absorbers and (ii) not so crowded in velocity space as the PAL absorbers. Indeed, there are many NALs detected in the spectra of both images A and B of SDSS J1029+2623. Their origin is not only the outflowing wind (*intrinsic* NALs, hereafter) but also cosmologically intervening gas such as foreground galaxies and the IGM (*intervening* NALs, hereafter). Although it has been traditionally believed that many NALs that fall within 5,000 km s^{-1} of the quasar emission redshift (termed *associated* absorption lines or AALs) are physically associated with the quasar (e.g., Weymann et al. 1979), we can separate intrinsic NALs from intervening ones more effectively by performing partial coverage analysis. In order to form a global picture of the outflowing wind, we need to understand the physical conditions of NAL absorbers (i.e., highly accelerated gas) as well as PAL absorbers (i.e., weakly accelerated gas).

In this paper, we present the results from our new spectroscopic observation of SDSS J1029+2623 taken with the Very Large Telescope (VLT), which enables us for the first time to identify *intrinsic* NALs in a high quality spectrum of this object. In §2, we describe the observations and data reduction. The methods used for absorption line detection and covering factor analysis are outlined in §3. The results and discussion are presented in §4 and §5. Finally, we summarize our results in §6. We use a cosmology with H_0=70 km s^{-1} Mpc^{-1}, Ω_m=0.3, and Ω_Λ=0.7 throughout the paper.

2. OBSERVATIONS

We acquired high resolution spectra of the brightest two of the three lensed images of SDSS J1029+2623, A and B with V = 18.72 and 18.67 mags, with the VLT using the Ultraviolet and Visual Echelle Spectrograph (UVES) in queue mode (ESO program 092.B-0512(A)). The observations were performed from 2014 January 28 to February 26 (epoch E2, hereafter), which is ∼4 years after the first observation on 2010 February 10 (epoch E1, hereafter; Misawa et al. 2013), and ∼2 months before the third observation on 2014 April 4 (epoch E3, hereafter; Misawa et al. 2014b) with Subaru using the High Dispersion Spectrograph (HDS). We used a slit width of 1.″2, corresponding to $R \sim$ 33,000, while Misawa et al. (2013, 2014b) took $R \sim$ 30,000 and 36,000 spectra using Subaru/HDS. The wavelength coverage is 3300–6600 Å in the 390/564 nm setting, which covers the O VI, N V, Si IV, and C IV doublets as well as the Lyα absorption line at $z_{\rm abs} \sim z_{\rm em}$. We also adopted 2×2 pixel binning in both the spatial and dispersion directions to increase the S/N ratio. The total integration time is 26,670s and the final S/N ratio is about 23 pix^{-1} around 4700Å for both images.

We reduced the data to extract the one-dimensional spectra in a standard manner using the UVES Common Pipeline Library (CPL release 6.6). We could not separate the third image (image C, V = 20.63) from image B completely because the typical seeing of our observation (∼ 1.″0–1.″8) was comparable to the separation angle between images B and C ($\theta \sim 1.''85$)[15].

Table 1 gives a log of the current observation with VLT/UVES as well as our past observations with Subaru/HDS, in which we list the target name, date of observation, telescope/instrument used, spectral resolution, total exposure time, and signal-to-noise ratio (S/N). The S/N is evaluated around 4700 Å, close to the C IV mini-BAL. In Figure 1, we show normalized spectra over the full wavelength range of our observations for images A and B. These spectra were binned every 0.5Å for display purposes, and the 1σ errors are also shown.

3. DATA ANALYSIS

[14] The time delay between images A and B is $\Delta t_{\rm AB} \sim 774$ days in the sense of A leading B, while the time delay between images B and C $\Delta t_{\rm BC}$ is only a few days (Fohlmeister et al. 2013).

[15] On the other hand, a flux contamination from the image C is almost negligible in the image B spectrum because the former is much fainter than the latter.

First, using the line detection code SEARCH, written by Chris Churchill, we detect all absorption features whose confidence level is greater than 5σ in the normalized spectrum of each lensed image. We then identify N V, C IV, and Si IV doublets in the regions from $-1{,}000$ km s^{-1} to 5,000 km s^{-1} (N V), from $-1{,}000$ km s^{-1} to 70,000 km s^{-1} (C IV), and from $-1{,}000$ km s^{-1} to 40,000 km s^{-1} (Si IV) around the corresponding emission lines, with the maximum velocity set in order to avoid the Lyα forest[16]. We also search for the Mg II doublet in the whole range of the spectra. Absorption troughs that are separated by nonabsorbed regions are considered to be separate lines. In total, 4 Mg II, 19 C IV, 2 N V, and 7 Si IV doublets are identified in the image A spectrum, while 3 Mg II, 22 C IV, 2 N V, and 7 Si IV doublets are identified in the image B spectrum. The equivalent widths of both blue and red members of doublets are measured for each line by integrating across the absorption profile and these are listed in Table 2. We also searched for 10 single metal lines (O I λ1302, Si II λ1190, Si II λ1193, Si II λ1260, Si II λ1527, Al II λ1671, C II λ1036, C II λ1335, Si III λ1207, and C III λ1548) as well as Lyα and Lyβ and detected about 200 lines at the same redshift as the doublet lines. These are summarized in Table **??**. Other single lines or unidentified lines are not shown in Figure 1 and Tables 1–**??** even if they are detected at a confidence greater than 5σ.

3.1. *dN/dz Analysis*

One of the important properties of intrinsic NALs is a number density excess of high-ionization doublets per unit redshift (i.e., dN/dz; Hamann et al. 1997a, and references therein). In order to compare the dN/dz from our spectra with those from our previous study based on 37 quasar spectra (Misawa et al. 2007a), we construct a complete sample including only NALs whose blue doublet members would be detected even in the lowest S/N spectrum in Misawa et al. (2007a). The corresponding lower limits of rest-frame equivalent widths (EWs) are $\mathrm{EW}^{\mathrm{rest}}_{\mathrm{min}} = 0.056$ Å, 0.038 Å, and 0.054 Å for C IV, N V, and Si IV, respectively. Here, the values of $\mathrm{EW}^{\mathrm{rest}}_{\mathrm{min}}$ depend on the S/N ratio of the observed spectrum as

$$EW^{\mathrm{rest}}_{\mathrm{min}} = \frac{-U^2 + U\sqrt{U^2 + 4(\mathrm{S/N})^2(M_L^2 M_c^{-1} + M_L)}}{2(\mathrm{S/N})^2(1+z_{abs})} \times \Delta\lambda(\mathring{A}), \quad (1)$$

where U is the confidence level of the EW defined as $\mathrm{EW}/\sigma(\mathrm{EW})$, and M_L and M_C are the numbers of pixels over which the equivalent width and the continuum level are determined (Young et al. 1979; Tytler et al. 1987). Using equation (1), we confirm that the S/N of our VLT spectra is always larger than the required values except for the region between $\lambda_{\mathrm{obs}} \sim 4500$ – 4525 Å (Figure 2). After removing weak NALs with $\mathrm{EW}^{\mathrm{rest}} < \mathrm{EW}^{\mathrm{rest}}_{\mathrm{min}}$, we have 12 C IV, 2 N V, and 3 Si IV doublets in image A spectrum and 11 C IV, 2 N V, and 3 Si IV doublets in the image B spectrum. We will call this the "homogeneous" NAL sample, hereafter. Following Misawa et al. (2007a), we also combined multiple NALs lying within 200 km s^{-1} of each other into a single NAL "system" because clustered lines are probably not independent even if they have a cosmologically intervening origin (e.g., Sargent, Steidel, & Boksenberg 1988).

All identified doublets (including both the homogeneous and inhomogeneous NAL samples) are listed in Table 2, in which multiple NALs within 200 km s^{-1} of each other are separated by horizontal lines. The table gives the ion name (*ion*), flux-weighted absorption redshift (z_{abs}), ejection velocity (v_{ej}) supposing they originate in the outflow, rest frame EWs of blue and red members of the doublet ($\mathrm{EW}^{\mathrm{rest}}_{\mathrm{b}}$, $\mathrm{EW}^{\mathrm{rest}}_{\mathrm{r}}$), identification number in Figure 1 (ID), reliability class of intrinsic lines (described later), ionization class (described later), and velocity difference from the first doublet at the lowest redshift in each absorption system (Δv). Table **??** summarizes other information including the flux-weighted line width of each system on a velocity scale, $\sigma(v)$, as defined in Misawa et al. (2007a), and other transitions that are detected at the same redshift, as well as the column density ($\log N$), Doppler parameter, b, and covering factor, C_{f}, for each absorption component in the system.

3.2. *Partial Coverage Analysis*

Among several criteria, i) time variability, ii) partial coverage, and iii) line locking are the most reliable properties to distinguish intrinsic NALs from intervening NALs (Barlow & Sargent 1997; Hamann et al. 1997a, and references therein). When compared with broad intrinsic absorption lines, intrinsic NALs are less likely to vary (Misawa et al. 2014a; Chen et al. 2015) and when they do vary, their variation amplitude is small (Wise et al. 2004; Misawa et al. 2014a). Therefore, the variability criterion does not offer an efficient way of identifying intrinsic NALs.

Partial coverage analysis is quite useful for our spectra because the resolving power is high enough to deblend NALs into multiple components. Using the Voigt profile fitting code MINFIT (Churchill 1997; Churchill et al. 2003), we deblended NALs into 86 and 91 components in images A and B, respectively. We do not include the Si IV NAL at $z_{\mathrm{abs}} = 1.8909$ because the blue and red members of the doublet are both blended with other lines. With MINFIT, we fit each NAL profile using the redshift (z), column density ($\log N$ in cm^{-2}), Doppler parameter (b in km s^{-1}), and covering factor (C_{f}) as free parameters. The covering factor (C_{f}) is the fraction of photons from the background source that pass through the absorber. If the background source is uniformly bright, then C_{f} also represents the fraction of the background source (i.e., the continuum source and/or broad emission line regions, BELRs) that is occulted by foreground absorbers along our sightline. If C_{f} is less than unity, it is likely that the absorbers are part of a quasar outflow because cosmologically intervening absorbers like substructures in foreground galaxies and the IGM are less likely to have internal structures as small as a size of the background flux sources (e.g., Wampler et al. 1995; Barlow & Sargent 1997). The covering factor is evaluated in an unbiased manner as

$$C_f = \frac{(R_r - 1)^2}{1 + R_b - 2R_r}\ , \quad (2)$$

where R_b and R_r are the residual (i.e., unabsorbed) fluxes

[16] Here, we define the velocity offset as positive for blueshifted NALs from the quasar emission redshift that is determined from Mg II emission line (Inada et al. 2006).

of the blue and red members of a doublet in the normalized spectrum (c.f., Hamann et al. 1997b; Barlow & Sargent 1997; Crenshaw et al. 1999). If MINFIT gives unphysical covering factors for some components, e.g., negative or greater than 1, we rerun the code assuming $C_{\rm f} = 1$ only for those components because the $C_{\rm f}$ values are very sensitive to continuum level errors, especially for full coverage doublets (Misawa et al. 2005). In addition to the *fitting* method above, we evaluate $C_{\rm f}$ values for each *pixel* as Ganguly et al. (1999) did (*pixel-by-pixel* method). The fitting results by both methods are shown in Figure 3 and the fit parameters by the fitting method are summarized in Table **??**. We have confirmed that the $C_{\rm f}$ values provided by the two methods are in good agreement with each other.

4. RESULTS

4.1. *Narrow Absorption Lines (NALs)*

Using our NAL sample toward the lensed images of SDSS J1029+2623, we perform several statistical analyses. In these analyses, in order to avoid any possible biases we do not include the two C IV NALs at $z_{\rm abs} \sim 1.9322$ and 1.9788 that are covered in the Subaru spectrum (Misawa et al. 2013) but not covered by our VLT data.

4.1.1. *dN/dz analysis*

In Table 4, we summarize the number density of homogeneous NAL systems per unit redshift (dN/dz) or per unit velocity offset from the quasar (dN/dβ) for C IV, N IV, and Si IV, along with the Poisson noise in these quantities (Gehrels 1986). All systems are also classified into one of two categories according to the offset velocity from the quasar; associated absorption lines (AALs) with $v_{\rm ej} \leq$ 5,000 km s^{-1}, and non-AALs with $v_{\rm ej} >$ 5,000 km s^{-1}, following Misawa et al. (2007a). We found that the dN/dz values for C IV, N V, and Si IV toward this one quasar, SDSS J1029+2623, are larger than the average values in the larger sample of Misawa et al. (2007a) by factors of $\sim$3, $\sim$6, and $\sim$2, respectively, although this enhancement is not statistically significant because of the small number of NALs in our spectra. Because Misawa et al. (2007a) discovered that at least $\sim$20% of C IV NALs originate from winds based on partial coverage analysis, statistically we expect to detect two or more intrinsic C IV NALs among $\sim$10 homogeneous C IV NALs in the spectra of images A and B.

4.1.2. *Intrinsic or Intervening NALs*

High-velocity NALs blueshifted with $v_{\rm ej} > 1000$ km s^{-1} are expected to be outside of the range of velocities where BELs are found, and thus, they absorb mostly continuum light. The existence of partial coverage in high-velocity NALs suggests that the size of absorbers is comparable to or smaller than the continuum source (i.e., $d_{\rm cloud} \leq R_{\rm cont}$). Following Misawa et al. (2007a), we separate all NALs (including those in the inhomogeneous sample) into three classes (classes-A, B, and C) based on partial coverage analysis, where class-A includes NALs most reliably classified as intrinsic while class-C includes NALs that are consistent with full coverage or that cannot be classified. Class-B contains NALs that show line-locking, which is a signature of a radiatively driven outflowing wind and is only detectable if our sightline is approximately parallel to the gas motion, as often seen in NALs (e.g., Benn et al. 2005; Bowler et al. 2014). Class-B also contains systems that have tentative evidence for partial coverage. As a result, 4 C IV NALs (including PALs) are classified as intrinsic (two class-A and two class-B) among the 12 C IV NALs in the homogeneous sample from the spectrum of image A, while 3 C IV NALs are classified as intrinsic (two class-A and one class-B) among 11 NALs in the spectrum of image B. The fraction of intrinsic NALs (27 – 33%) is somewhat larger than the average value of $\sim$20% (Misawa et al. 2007a), although our sample size is small. If we include the inhomogeneous sample, 5 C IV NALs are classified as 3 class-A and 2 class-B among 19 NALs toward image A, while 9 out of 22 C IV NALs are classified into 4 class-A and 5 class-B NALs toward image B. In addition to intrinsic C IV NALs, we detected two class-B Si IV NALs only toward image A in homogeneous sample, and three class-B Si IV NALs in each of the image A and B spectra after including systems from the inhomogeneous sample. It is also noteworthy that we detect a large number of line-locked NALs: 2 C IV and 3 Si IV NALs in image A and 5 C IV and 3 Si IV NALs in image B, while only five systems are line-locked among 138 homogeneous NALs toward 37 quasars (Misawa et al. 2007a). This result strongly suggests that our sightline toward the central source is almost parallel to the outflowing streamline.

4.1.3. *Ionization Conditions*

The outflowing winds in the vicinity of the flux source are probably more highly ionized than most intervening absorbers due to strong UV radiation from the continuum source, although it depends on the gas density of the absorbers. Indeed, a high ionization state has been used as one indicator of the intrinsic properties of absorbers (Hamann et al. 1997a, and references therein). Broad absorption lines (BALs) are often classified into three categories according to their ionization level: high-ionization BALs (HiBALs), low-ionization BALs (LoBALs), and extremely low-ionization BALs showing Fe II lines (FeLoBALs) (Weymann et al. 1991). A similar classification has also been performed for NALs (Bergeron et al. 1994; Misawa et al. 2007a). Motivated by the literature, we classify our NALs into three categories, based on the detection of absorption lines in low (ionization potential; IP $<$ 25 eV), intermediate (IP = 35 – 50 eV), and high (IP $>$ 60 eV) ionization levels[17]. Interestingly, some class-A NAL systems include low ionization lines (see Table 2), which suggests that intrinsic NAL absorbers have multiple phases with different ionization states, as noted in Misawa et al. (2007a).

4.1.4. *Similarities in NALs between Sightlines*

Here, we present a new method of identifying intrinsic NALs by exploiting our multi-sightline observation. If NALs with similar line profiles are detected at the same redshift toward two sightlines, the corresponding

[17] An important caveat here is that we do not necessarily detect all absorption lines because of the detection limits due to line strength, observed wavelength coverage, and line blending (e.g., in Lyα forest).

absorber must have a size larger than the physical distance between the two sightlines. The absorber also cannot have any internal structures on the scale of the sightline separation. Although foreground galaxies and IGM structures also can cover both sight lines (whose physical separation is ∼kpc or ∼Mpc scale), they usually have significant internal velocity structures on those scales, as often seen in the spectra of lensed quasars (e.g., Ellison et al. 2004). Only intrinsic absorbers can satisfy the requirement of having very similar profiles because their sizes can be larger than the sightline separation (e.g., sub-parsec scale) if they are at a small distance from the flux source (e.g., $r < 1$ kpc). Based on the ejection velocity distribution of class-A, B, and C NALs (Figure 4), in Figure 5 we summarize the distribution of velocity differences between NALs and PALs in the two sightlines (Δv) for systems within $\Delta v \leq 200$ km s^{-1} between the two sightlines. The distribution is almost uniform up to $\Delta v \sim 200$ km s^{-1} with a clear peak near $\Delta v \sim 0$ km s^{-1}. Among eight NAL pairs with $\Delta v \leq 10$ km s^{-1}, four are C IV and N V PALs at $z_{\rm abs} \sim z_{\rm em}$, which we will discuss later. The other four NAL pairs are C IV NALs at $z_{\rm abs}$ ∼ 1.8909, 2.1349, and 2.1819, and a Si IV pair at $z_{\rm abs}$ ∼ 1.8909. Although the velocity shift is very small for these NAL pairs, their line profiles are clearly different as compared in Figure 6. This means our two sightlines go through different absorbers or different regions of a single absorber. In either event, we cannot conclude that these are intrinsic NALs based only on this analysis. On the other hand, it is intriguing that no NAL pairs that are classified into class-A/B have a common ejection velocity or line profile. For example, the C IV NALs at $z_{\rm abs} = 1.7652$ toward image A and at $z_{\rm abs} = 1.7650$ toward image B are both classified as class-A NALs. Although their ejection velocities are very close each other, their line centers and profiles are obviously different, as shown in Figure 7. We also note that the difference is remarkable in all three epochs (see Figure 8). This means the multi-sightline scenario (i.e., that two sightlines pass through different regions of the outflow) is also applicable for intrinsic NALs with large ejection velocity as well as for PALs as already confirmed in Misawa et al. (2013, 2014b).

4.1.5. *Time Variability of NALs*

Because of the lower data quality (S/N ∼ 10 pixel^{-1}) and narrower effective wavelength coverage of the Subaru/HDS spectra taken in epochs E1 and E3, we cannot monitor NALs for time variability analysis with only a few exceptions. As an example, we compare spectra obtained at three epochs around the strong C IV NALs at $z_{\rm abs} = 1.8909$–1.9138 (ID = 35–44) in image A and C IV NALs at $z_{\rm abs} = 1.8909$–1.9119 (ID = 41–48) in image B as shown in Figure 9. These NALs are obviously not variable, which is consistent with the past result that NALs with large ejection velocities are rarely variable (Chen et al. 2015).

4.2. *Proximity Absorption Lines (PALs)*

The absorption line group at $z_{\rm abs} \sim z_{\rm em}$ with an ejection velocity of $v_{\rm ej} < 1000$ km s^{-1} has already been observed twice in 2010 February (epoch E1) and 2014 April (epoch E3) with Subaru/HDS. Its origin is probably in the outflowing gas because: i) there is evidence for partial coverage (e.g., there exists a clear residual flux at the bottom of the Lyα and N V absorption lines even though they appear to be saturated.), ii) the profiles are variable, and iii) the profiles show signatures of line-locking (Misawa et al. 2013, 2014b). The most important result from these past observations is that the absorption profiles of the Lyα, N V, and C IV PALs in the spectra of images A and B are clearly different, especially for lines at $v_{\rm ej} < 0$ km s^{-1} (see Figure 10). There are at least three possible origins for the difference: a) a micro-lensing effect, b) time delay between the images, and c) different absorber structure along the different sightlines. Among these, the first idea is immediately rejected because the lensed images show a common ratios between the radio, optical, and X-ray fluxes (Ota et al. 2012; Oguri et al. 2012), which is not expected for micro-lensing. We can also reject the time delay effect because the variability is almost negligible between epochs E1 and E3 (Misawa et al. 2014b). A difference in column density between the two sightlines is the only acceptable explanation. To our knowledge, this is the first time that an outflowing wind has been observed along multiple sightlines. Hereafter, we call the PALs at $v_{\rm ej} < 0$ km s^{-1} (showing sightline difference) narrow PALs and those at $v_{\rm ej} > 0$ km s^{-1} (showing similar line profiles between sightlines) broad PALs (see Figure 10).

Our observation with VLT/UVES not only gives an additional epoch for monitoring the PALs but enables us to study the detailed velocity structure of PALs using higher quality spectra with a S/N ratio double that of the past observations with Subaru. We first confirm the line-locking pattern in velocity plots of the C IV PAL as shown in Figure 11, which was already noted in Misawa et al. (2013). Like the other NAL absorbers, the PAL absorbers also appear to be outflowing almost parallel to our sightline. We also reconfirm that the C IV PALs became shallower (i.e., decreasing in equivalent width) over a large velocity range of the profile between epochs E1 and E2/E3 (see Figure 11) at $\Delta t_{\rm rest}$ ∼1.3 years in the quasar rest-frame. However, these lines are almost stable on the shorter time scales of $\Delta t_{\rm rest}$ ∼0.05 years between epochs E2 and E3. The broad spectral coverage of the VLT/UVES spectra allows us to detect for the first time the O VI doublet corresponding to the PAL absorber (see Figure 10). There is also a hint of the Si IV doublet detected, but it appears blended with other lines at lower redshift.

4.2.1. *Comparison of Covering Factors*

In addition to line profiles and strengths, we also compare covering factors for the clean part of the C IV and N V PALs in the three epochs. The fitting parameters to the PALs in epoch E2 with MINFIT are summarized in Table **??**. The total column densities of C IV and N V PALs after summing all Voigt components are $\log(N_{\rm NV}/{\rm cm}^{-2}) = 15.62$ and $\log(N_{\rm CIV}/{\rm cm}^{-2}) = 15.90$ in image A and 16.04 and 15.89 in image B spectrum. These values are all consistent with the corresponding values that we measured in epoch E1 (Misawa et al. 2013) with differences of a factor of ≤ 2. Because all PALs have small offset velocities and are located on the BELs in the spectra, we should consider the BELRs as well as the contin-

uum source as the background flux source. Because the C IV PAL is partially self-blended (i.e., blending of the blue members of one doublet with the red member of another doublet), we can compare covering factors effectively only for the narrow PALs at $v_{\rm ej} \sim -100$–0 km s^{-1} (corresponding to $\Delta v \sim 400$–500 km s^{-1} in Figure 12), for which self-blending is negligible[18].

We show the fitting results for the PALs in epoch E2 in Figure 12 and Table **??**. The average covering factors of C IV and N V at $v_{\rm ej} \sim -100$–0 km s^{-1} (i.e., $\Delta v \sim 400$–500 km s^{-1} in Figure 12) are $C_{\rm f} = 0.47\pm0.03$ and 0.58 ± 0.05 toward image A, and $C_{\rm f} = 0.23\pm0.02$ and 0.39 ± 0.08 toward image B. These values are all consistent with the corresponding values in epoch E1 toward image A ($C_{\rm f} = 0.47\pm0.05$ and 0.61 ± 0.07) and image B ($C_{\rm f} \sim 0.2$ and 0.35 ± 0.05)[19] and in epoch E3 toward image A ($C_{\rm f} = 0.45\pm0.09$ and 0.54 ± 0.09) and image B ($C_{\rm f} = 0.20\pm0.05$ and 0.34 ± 0.19). Thus, covering factors are not variable at least on a timescale of $\Delta t_{\rm rest} \sim 1.3$ years.

The N V PALs all have larger $C_{\rm f}$ values than that for C IV, which is consistent with past results that higher ionization transitions tend to have larger coverage fractions (e.g., Petitjean & Srianand 1999; Srianand & Petitjean 2000; Misawa et al. 2007a; Muzahid et al. 2015). This result suggests that i) the size (i.e., distance from the central black hole) of the N V BELR is smaller than that of the C IV BELR, and/or ii) the size of the N V absorbers is larger than that of the C IV absorbers. It is also interesting that the PALs in the image A spectrum always have larger $C_{\rm f}$ values than those in the image B spectrum, which is additional evidence for variations in the structure along multiple sightlines.

5. DISCUSSION

5.1. *Velocity anisotropies in NAL absorbers*

Line-locking is seen in both NALs and PALs, thus we are likely to be observing the quasar almost along the direction of the outflow. Nonetheless, we discovered a velocity difference between the two sightlines (see Table 2). Given the redshifts of the lens ($z_{\rm l} = 0.58$; Oguri et al. 2008) and the source ($z_{\rm s} = 2.197$) the separation angle of the light rays that form images A and B, as seen from the source[20], is $\theta' \sim 14\farcs6$. This velocity gradient suggests that the outflowing wind has internal velocity anisotropies on a scale of $\sim$1 km s^{-1} arcsec^{-1} on average. Indeed, the hydrodynamic simulations of Proga & Kallman (2004) show this type of internal velocity variations. A recent radiation-MHD simulation by Takeuchi et al. (2013) also reproduced such velocity variations over a typical spatial scale of $\sim 5\times10^{-4}$ pc. This is consistent with the size of NAL absorbers, which is also comparable to the size of the continuum source ($\sim 2.5\times10^{-4}$ pc; Misawa et al. 2013). However, we should note that the velocity variations in the simulations are found in the inner part of the wind at distances of $\sim 50 R_{\rm g}$ from the center.

The velocity distribution of intrinsic NALs that are classified into Class-A or B appears to cluster around values of $v_{\rm ej} \sim$ 59,000, 43,000, and 29,000 km s^{-1}, except for two intrinsic NALs at $v_{\rm ej} \sim$ 49,500 km s^{-1} (class-A) and $\sim$ 8,500 km s^{-1} (class-B) in the image B spectrum (Figure 4). These clustering patterns are reminiscent of the filamentary structures obtained by numerical simulations (e.g., Proga, Stone, & Kallman 2000). If these patterns are indeed due to filamentary structures, there should exist some velocity anisotropies within them. Velocity dispersions in the three intrinsic NAL clusters are $\delta v \sim$ 900, 260, and 1200 km s^{-1} respectively, which correspond to about 1.6%, 0.6%, and 4.0% of their average ejection velocity.

5.2. *Ionization condition in PAL absorbers*

The Lyα, C IV, and N V PALs have been monitored at three epochs (E1, E2, and E3) between 2010 February and 2014 April. Between epochs E1 and E2/E3, C IV PALs show a clear variation in their strength (i.e., depth). There are several possible reasons for this time variability: (a) gas motion across our line of sight (e.g., Hamann et al. 2008; Gibson et al. 2008; Muzahid et al. 2015), (b) changes in the ionization state of the absorber (e.g., Hamann et al. 2011; Misawa et al. 2007b), and (c) redirection of photons around the absorber by scattering material (e.g., Lamy & Hutsemékers 2004; Misawa et al. 2010). Among these, the first scenario can be rejected because all absorption components in the C IV PAL vary in concert, which requires the implausible situation in which all clouds cross our sightline simultaneously (c.f. Misawa et al. 2007b). The third scenario is also less likely because it requires a variation in the covering factor while the $C_{\rm f}$ values remain almost stable both in C IV and N V PALs between epochs E1 and E2/E3. Thus, only the scenario involving a change in ionization state deserves further investigation. This scenario is further separated into two variants: i.e., C^{3+} ions are ionized to C^{4+} or they recombine to C^{2+}. Both variants of this scenario can explain the decreasing EW of the C IV PALs. Without knowing an absorber's ionization parameter[21], we cannot tell which one is more likely. If the latter variant applies, we can place constraints on the electron density and the distance from the ionizing photon source by the same prescription as used in Narayanan et al. (2004), taking the variability time scale as an upper limit to the recombination time. Based on the observation that the C IV PALs vary between epochs E1 and E3 over $\Delta t_{\rm obs} = 1514$ days (i.e., $\Delta t_{\rm rest} = 474$ days)[22] we can place a lower limit on the

[18] Negative ejection velocity for these components could be due to our underestimation of these values because the emission redshift is determined from broad UV emission lines, as done for this quasar by Inada et al. (2006), which are systematically blueshifted from the systemic redshift that is measured by narrow, forbidden lines (see, e.g., Corbin 1990; Tytler & Fan 1992; Brotherton et al. 1994; Marziani et al. 1996) by about 260 km s^{-1}.

[19] Because no absorption component was used for C IV PAL at $v_{\rm ej} \leq 0$ km s^{-1} in the epoch E1 spectrum (Misawa et al. 2013), we adopt an average line depth for this region as a covering factor.

[20] The separation angle as seen by the source is given by $\theta' = (D_{\rm ol}/D_{\rm sl}) \times \theta$, where θ is the observed separation angle of the images ($22\farcs5$) and $D_{\rm ol}$ and $D_{\rm sl} = ((1+z_s)/(1+z_l)) \times D_{\rm ls}$ are angular diameter distances from the observer to the lens and from the source to the lens, respectively.

[21] The ionization parameter U is defined as the ratio of hydrogen ionizing photon density (n_γ) to the electron density (n_e).

[22] We compare spectra in epochs E1 and E3 instead of epochs E1 and E2 because the E2 observation spans the time range 2014 January 28 to February 26, which gives an additional uncertainty for measuring the variation time scale.

electron density of the absorber as $n_e > 8.7 \times 10^3$ cm^{-3}, and an upper limit on the distance from the flux source as $r < 620$ pc, assuming $U \sim 0.02$, the value at which the C IV and N V ions are close to the optimal ionization states for those elements (e.g., Hamann et al. 1995).

5.3. *Global Picture of the Outflow from SDSS J1029+2623*

In Table 5, we summarize the physical properties of broad PALs, narrow PALs, and intrinsic NALs. We also present a possible geometry of the outflow along our two sightlines in Figure 13 based on our previous constraints.

First, we see almost the same absorption profiles of Lyα, N V, and C IV PALs in the two lensed images except for a clear difference in the narrow PALs at $v_{\rm ej} \sim -100$–0 km s^{-1}. We also confirm that none of the intrinsic NALs have common absorption profiles between the images. These results suggest that the size of the broad PAL absorbers are larger than the projected separation between sightlines at the distance of the absorbers, $r\theta$, while the narrow PAL absorbers and NAL absorbers have sizes smaller than $r\theta$. Such common absorption profiles are, however, observable regardless of the absorber's size, if their distance from the flux source is smaller than the boundary radius $r_{\rm b}$ at which the two sightlines of lensed images become fully separated with no overlap (Misawa et al. 2013). The boundary distance is ∼3.5 pc for SDSS J1029+2623 if only the continuum source is counted. If we also consider the BELR (whose size is estimated to be ∼0.09 pc)[23] as the background source, $r_{\rm b}$ would be ∼1200 pc (see Figure 13).

We can also place constraints on the absorber size based on partial covering analysis. Intrinsic NALs with large ejection velocities have partial coverage, although they absorb only the continuum photons. This means their physical scale is comparable to or smaller than the size of the continuum source, $d_{\rm cloud} \leq 2.5\times10^{-4}$ pc. On the other hand, broad PAL absorbers cover almost entirely both the BELR and the continuum source, which means the size of the absorbers as a whole is comparable to or larger than the BELR size, ≥ 0.09 pc. Narrow PAL absorbers may consist of a number of small clumpy clouds because they show partial coverage.

In our VLT/UVES spectra, we detected high-ionization transitions like O VI and N V in the PAL systems, while the intrinsic NAL systems are in various ionization states, with or without high-ionization transitions, as already noted in the literature (e.g., Misawa et al. 2007a; Ganguly et al. 2013). Some C IV NAL absorbers also show N V transitions, while others do not. Because Lyα and N V in the PAL system are less variable than C IV and because N V has larger covering factor than C IV, the cross-section of Lyα and N V should be larger than that of C IV. PAL absorbers with strong O VI lines are probably located much closer to the ionizing flux source than NAL absorbers, although this conclusion depends on the density of the absorber.

It is well known that both broad and narrow absorption lines at $z_{\rm abs} \sim z_{\rm em}$ tend to vary (Wise et al. 2004; Misawa et al. 2014a), while NALs with large ejection velocities are rarely variable (e.g., Chen et al. 2015). Indeed, the PALs in our spectra are variable, while most of the C IV NALs are probably stable between the three epochs, as we observed for a few strong C IV NALs. Misawa et al. (2014a) suggest that broader absorption lines like the broad PALs can vary mainly due to a change in their ionization state while narrow absorption lines like narrow PALs and NALs vary primarily due to the gas motion transverse to our sightlines. The gas motion scenario could explain why narrow PALs are variable but high-velocity NALs are not. Based on the dynamical model of Murray et al. (1995) and more recent investigations (e.g., Misawa et al. 2005; Hall et al. 2011), the absorbers at larger distance from the center have small transverse (i.e., orbital) velocities compared to their radial velocities. If intrinsic NALs lie at larger distances than narrow PALs, their small transverse velocities would rarely lead to time variability, while the large transverse velocities of narrow PALs can lead to time variability more frequently.

[23] This is calculated by Misawa et al. (2013) based on the empirical equation in McLure & Dunlop (2004).

6. SUMMARY

In this study, we performed a spectroscopic observation for images A and B of the gravitationally lensed quasar SDSS J1029+2623, and monitored the absorption profiles in these spectra as well as in the previous two observations. Using high quality spectra taken with VLT/UVES, we detected intrinsic narrow absorption lines (NALs) as well as broader, proximity absorption lines (PALs), and fit models to the line profiles. Based on the results of our multi-sightline spectroscopy, we discuss a possible geometry and internal structure of the outflowing wind along our sightlines. Our main results are as follows.

- We detected 66 NALs, of which 24 are classified as *intrinsic* NALs (physically associated with the quasar) based on partial coverage analysis.
- Class-A and B NALs cluster at $v_{\rm ej} \sim$ 59,000, 43,000, and 29,000 km s^{-1}, which is reminiscent of the filamentary structures that are often obtained in numerical simulations.
- Our multiple sightline observation suggests that the size of the broad PAL absorbers are larger than the projected distance between sightlines ($r\theta$) while the narrow PAL absorbers and intrinsic NAL absorbers have sizes smaller than $r\theta$ if their radial distances are greater than the boundary distance.
- While PAL systems show only high ionization transitions, including O VI, intrinsic NAL systems show a wide range of ionization conditions with and without low ionization transitions like O I, Al II, and Si II, as noted in the literature.
- No class-A/B NALs (i.e., candidates for intrinsic NALs) have common absorption profiles in the two lensed images, which means that the outflow has an internal velocity structure whose typical spatial scale is smaller than the physical distance between the sightlines (i.e., $\leq r\theta$).
- Short-time variation in the PALs is probably due to a change in the ionization state of the gas. If this is the case, we can place a lower limit on the gas

density as $n_e \geq 8.7 \times 10^3$ cm^{-3} and an upper limit on the absorber's distance from the flux source as $r \leq$ 620 pc.

- Based on our best knowledge, we present a possible geometry of the outflow along our two sightlines, in which we identify different structures in the outflowing wind that can produce, respectively, broad PALs, narrow PALs, and NALs with large ejection velocities.

For further investigations of the outflow's internal structure, especially in the transverse direction, we should perform the same observations for image C of SDSS J1029+2623. We also aim to observe several lensed quasars with smaller separation angles ($\theta \sim 2''$) by a single massive galaxy to examine $\sim$10 times finer internal structure in an outflow, as already mentioned in Misawa et al. (2014b).

We thank the anonymous referee for comments that helped us improve the paper. We would like to thank Masamune Oguri, Poshak Gandhi, and Chris Culliton for their valuable comments. We also would like to thank Christopher Churchill for providing us with the MINFIT and SEARCH software packages. The research was supported by the Japan Society for the Promotion of Science through Grant-in-Aid for Scientific Research 15K05020, JGC-S Scholarship Foundation, and partially supported by MEXT Grant-in-Aid for Scientific Research on Innovative Areas (No. 15H05894). CS acknowledges support from CONICYT-Chile through Becas Chile 74140006. FEB acknowledges support from CONICYT-Chile (Basal-CATA PFB-06/2007, FONDECYT Regular 1141218, "EMBIGGEN" Anillo ACT1101) and the Ministry of Economy, Development, and Tourism's Millennium Science Initiative through grant IC120009, awarded to The Millennium Institute of Astrophysics, MAS. JCC and ME acknowledge support from the National Science Foundation through award AST-1312686.

REFERENCES

Arav, N., Borguet, B., Chamberlain, C., Edmonds, D., & Danforth, C. 2013, MNRAS, 436, 3286
Benn, C. R., Carballo, R., Holt, J., et al. 2005, MNRAS, 360, 1455
Barlow, T. A., & Sargent, W. L. W. 1997, AJ, 113, 136
Bergeron, J., et al. 1994, ApJ, 436, 33
Blandford, R.D. & Parne, D.G., 1982, MNRAS, 199, 883
Bowler, R. A. A., Hewett, P. C., Allen, J. T., & Ferland, G. J. 2014, MNRAS, 445, 359
Brotherton, M. S., Wills, B. J., Steidel, C. C., & Sargent, W. L. W. 1994, ApJ, 423, 131
Chartas, G., Eracleous, M., Dai, X., Agol, E., & Gallagher, S. 2007, ApJ, 661, 678
Chen, Z.-F., Gu, Q.-S., Chen, Y.-M., & Cao, Y. 2015, MNRAS, 450, 3904
Chelouche, D. 2003, ApJ, 596, L43
Churchill, C. W., Vogt, S. S., & Charlton, J. C. 2003, AJ, 125, 98
Churchill, C. W. 1997, Ph.D. Thesis, Univ. California, Santa Cruz
Corbin, M. R. 1990, ApJ, 357, 346
Crenshaw, D. M., Kraemer, S. B., Boggess, A., Maran, S. P., Mushotzky, R. F., & Wu, C.-C. 1999, ApJ, 516, 750
Gehrels, N. 1986, ApJ, 303, 336
Dorodnitsyn, A. V. 2009, MNRAS, 393, 1433
Dunn, J. P., Bautista, M., Arav, N., et al. 2010, ApJ, 709, 611
Ellison, S. L., Ibata, R., Pettini, M., et al. 2004, A&A, 414, 79
Elvis, M. 2000, ApJ, 545, 63
Emmering, R.T., Bladford, R.D., & Shlosman, I., 1992, ApJ, 385, 460
Everett, J. E., 2005, ApJ, 631, 689
Fohlmeister, J., Kochanek, C. S., Falco, E. E., et al. 2013, ApJ, 764, 186
Foltz, C., Wilkes, B., Weymann, R., & Turnshek, D. 1983, PASP, 95, 341
Gabel, J.R., Arav, N., & Kim, T.-S. 2006, ApJ, 646, 742
Ganguly, R., Lynch, R. S., Charlton, J. C., et al. 2013, MNRAS, 435, 1233
Ganguly, R., Bond, N. A., Charlton, J. C., et al. 2001, ApJ, 549, 133
Ganguly, R., Eracleous, M., Charlton, J. C., & Churchill, C. W. 1999, AJ, 117, 2594
Gibson, R. R., Brandt, W. N., Schneider, D. P., & Gallagher, S. C. 2008, ApJ, 675, 985
Green, P. J. 2006, ApJ, 644, 733
Hall, P. B., Brandt, W. N., Petitjean, P., et al. 2013, MNRAS, 434, 222
Hall, P. B., Anosov, K., White, R. L., et al. 2011, MNRAS, 411, 2653
Hamann, F., Chartas, G., McGraw, S., et al. 2013, MNRAS, 435, 133
Hamann, F., Kanekar, N., Prochaska, J. X., et al. 2011, MNRAS, 410, 1957
Hamann, F., Kaplan, K. F., Rodríguez Hidalgo, P., Prochaska, J. X., & Herbert-Fort, S. 2008, MNRAS, 391, L39
Hamann, F., & Sabra, B. 2004, AGN Physics with the Sloan Digital Sky Survey, 311, 203
Hamann, F., Barlow, T. A., Junkkarinen, V., & Burbidge, E. M. 1997a, ApJ, 478, 80
Hamann, F., Barlow, T. A., & Junkkarinen, V. 1997b, ApJ, 478, 87
Hamann, F., Barlow, T. A., Beaver, E. A., et al. 1995, ApJ, 443, 606
Inada, N., Oguri, M., Morokuma, T., et al. 2006, ApJ, 653, L97
Jannuzi, B. T., Hartig, G. F., Kirhakos, S., et al. 1996, ApJ, 470, L11
Joshi, R., Chand, H., Srianand, R., & Majumdar, J. 2014, MNRAS, 442, 862
Konigl, A., & Kartje, J. F. 1994, ApJ, 434, 446
Kurosawa, R. & Proga, D. 2009, ApJ, 693, 1929
Lamy, H., & Hutsemékers, D. 2004, A&A, 427, 107
Marziani, P., Sulentic, J. W., Dultzin-Hacyan, D., Calvani, M., & Moles, M. 1996, ApJS, 104, 37
McLure, R. J., & Dunlop, J. S. 2004, MNRAS, 352, 1390
Misawa, T., Charlton, J. C., & Eracleous, M. 2014a, ApJ, 792, 77
Misawa, T., Inada, N., Oguri, M., et al. 2014b, ApJ, 794, L20
Misawa, T., Inada, N., Ohsuga, K., et al. 2013, AJ, 145, 48
Misawa, T., Kawabata, K. S., Eracleous, M., Charlton, J. C., & Kashikawa, N. 2010, ApJ, 719, 1890
Misawa, T., Charlton, J. C., Eracleous, M., Ganguly, R., Tytler, D., Kirkman, D., Suzuki, N., & Lubin, D. 2007a, ApJS, 171, 1
Misawa, T., Eracleous, M., Charlton, J. C., & Kashikawa, N. 2007b, ApJ, 660, 152
Misawa, T., Eracleous, M., Charlton, J.C., & Tajitsu, A., 2005, ApJ, 629, 115
Murray, N., Chiang, J., Grossman, S. A., & Voit, G. M., 1995, ApJ, 451, 498
Muzahid, S., Srianand, R., Charlton, J., & Eracleous, M. 2015, arXiv:1509.07850
Muzahid, S., Srianand, R., Arav, N., Savage, B. D., & Narayanan, A. 2013, MNRAS, 431, 2885
Narayanan, D., Hamann, F., Barlow, T., Burbidge, E.M., Cohen, R.D., Junkkaribeb, V., & Lyons, R., 2004, ApJ, 601, 715
Nestor, D., Hamann, F., & Rodriguez Hidalgo, P. 2008, MNRAS, 386, 2055
Nomura, M., Ohsuga, K., Wada, K., Susa, H., & Misawa, T. 2013, PASJ, 65,
Oguri, M., Schrabback, T., Jullo, E., et al. 2012, arXiv:1209.0458
Oguri, M., Ofek, E. O., Inada, N., et al. 2008, ApJ, 676, L1
Ota, N., Oguri, M., Dai, X., et al. 2012, arXiv:1202.1645
Petitjean, P. & Srianand, R., 1999, A&A, 345, 73
Proga, D., & Kallman, T. R. 2004, ApJ, 616, 688
Proga, D., Stone, J. M., & Kallman, T. R., 2000, ApJ, 543, 686
Sargent, W.L.W., Boksenberg, A., & Steidel, C.C., 1988, ApJS, 68, 539
Springel, V., Di Matteo, T., & Hernquist, L. 2005, ApJ, 620, L79
Srianand, R. & Petitjean, P., 2000, A&A, 357, 414
Takeuchi, S., Ohsuga, K., & Mineshige, S. 2013, PASJ, 65, 88
Tytler, D., & Fan, X.-M. 1992, ApJS, 79, 1
Tytler, D., Boksenberg, A., Sargent, W. L. W., Young, P., & Kunth, D., 1987, ApJS, 64, 667

Vestergaard, M., 2003, ApJ, 599, 116
Wampler, E. J., Chugai, N. N., & Petitjean, P. 1995, ApJ, 443, 586
Weymann, R. J., Morris, S. L., Foltz, C. B., & Hewett, P. C. 1991, ApJ, 373, 23
Weymann, R. J., Williams, R. E., Peterson, B. M., & Turnshek, D. A. 1979, ApJ, 234, 33
Wise, J. H., Eracleous, M., Charlton, J. C., & Ganguly, R. 2004, ApJ, 613, 129
Young, P. J., Sargent, W. L. W., Boksenberg, A., Carswell, R. F., & Whelan, J. A. J., 1979, ApJ, 229, 891

TABLE 1
Log of Observations

Target	Obs Date	Instrument	R	$T_{\rm exp}$ (sec)	S/N[a] (pix^{-1})	Reference[b]
SDSS J1029+2623 A	2010 Feb 10	Subaru/HDS	30000	14400	13	1
	2014 Jan 28 – Feb 3	VLT/UVES	33000	26670	23	2
	2014 Apr 4	Subaru/HDS	36000	11400	14	3
SDSS J1029+2623 B	2010 Feb 10	Subaru/HDS	30000	14200	13	1
	2014 Feb 4 – 26	VLT/UVES	33000	26670	23	2
	2014 Apr 4	Subaru/HDS	36000	11400	14	3

[a] Signal to noise ratio at $\lambda_{\rm obs} \sim 4700$Å.
[b] References. (1) Misawa et al. 2013, (2) This paper, (3) Misawa et al. 2014b.

TABLE 2
Absorption Systems with Doublet Lines

Image A								Image B								
Ion	z_{abs}	v_{ej} (km s^{-1})	$EW_b^{rest\,a}$ (Å)	$EW_r^{rest\,b}$ (Å)	ID	Class-1^c	Class-2^d	Ion	z_{abs}	v_{ej} (km s^{-1})	$EW_b^{rest\,a}$ (Å)	$EW_r^{rest\,b}$ (Å)	ID	Class-1^c	Class-2^d	Δv^e (km s^{-1})
Mg II	0.5111	190431	0.604±0.008	0.495±0.008	27,29	C1	L									
								Mg II	0.5124	190276	0.095±0.004	0.052±0.004	31,32	C3	L	0.0
Mg II	0.5125	190265	0.221±0.005	0.145±0.004	28,30	C1	L									+19.8
								Mg II	0.6731	171003	1.689±0.008	1.444±0.008	49,50	C1	L	
Mg II	0.9176	141245	0.193±0.002	0.120±0.002	61,63	C3	L									0.0
								Mg II	0.9184	141157	0.186±0.005	0.092±0.005	67,68	C1	L	+125.1
Mg II	0.9187	141116	1.472±0.006	1.366±0.006	62,64	C1										+172.0
								C IV	1.6085	60206	0.035±0.002	0.026±0.002	7,10	B2	H	
								C IV	1.6149	59493	0.105±0.004	≤0.132	12,13	B2	IH	0.0
C IV	1.6151	59472	0.308±0.003	0.297±0.003	8,11	B2,H	IH									+22.9
C IV	1.6160	59378	0.047±0.003	≤0.033	9,12	C2										+126.2
								C IV	1.6221	58699	≤0.284	0.144±0.002	16,20	C2,H	H	0.0
C IV	1.6230	58601	≤0.512	0.190±0.007	16,18	B2,H	H									+103.0
								C IV	1.6253	58350	0.021±0.002	0.014±0.002	18,22	B2	H	
								C IV	1.6556	55033	0.133±0.004	0.081±0.003	25,26	C1	H	
								C IV	1.6924	51029	0.084±0.002	0.046±0.002	27,28	C2	H	0.0
C IV	1.6930	50965	0.498±0.005	0.185±0.007	23,24	C2,H	LIH									+66.8
								C IV	1.7065	49509	0.042±0.002	0.032±0.002	29,30	A2	H	
C IV	1.7212	47932	0.493±0.005	0.053±0.004	25,26	C2,H	H									
								C IV	1.7617	43596	0.010±0.002	0.011±0.002	33,36	C3	LIH	0.0
								C IV	1.7627	43496	0.094±0.002	0.066±0.002	34,37	B1		+108.6
								C IV	1.7650	43250	0.041±0.002	0.022±0.002	35,38	A2	H	0.0
C IV	1.7652	43224	0.047±0.002	0.035±0.002	31,32	A2	LIH									+21.7
C IV	1.8909	30091	0.355±0.004	0.309±0.003	35,37	C1,H	LIH									0.0
								C IV	1.8909	30088	0.456±0.006	≤0.501	41,43	C2,H	IH	0.0
Si IV	1.8909	30088	0.181±0.003	≤0.268	5,10	B2,H										0.0
								Si IV	1.8909	30087	0.121±0.004	0.119±0.004	5,14	B2		0.0
								Si IV	1.8944	29737	0.380±0.005	≤0.383	6,17	C2,H	LIH	0.0
								C IV	1.8945	29723	≤0.669	≤0.592	42,44	C2,H		+10.4
C IV	1.8949	29686	0.413±0.004	0.318±0.004	36,39	C2,H	LIH									+51.8
Si IV	1.8949	29685	0.137±0.003	≤0.464	6,14	B2										+51.8
								Si IV	1.8975	29413	0.032±0.002	0.019±0.002	8,19	B2	LIH	0.0
C IV	1.8982	29343	0.193±0.004	0.146±0.005	38,40	C1,H	IH									+72.5
Si IV	1.8982	29342	0.029±0.003	0.013±0.002	7,17	C2										+72.5
								Si IV	1.9016	28991	0.162±0.003	0.142±0.002	9,21	C1,H	LIH	0.0
								C IV	1.9019	28964	0.457±0.005	0.363±0.006	45,46	C1,H		+31.0
								Si IV	1.9024	28917	0.023±0.002	0.013±0.002	11,23	B2		+82.7
C IV	1.9115	27981	0.572±0.008	0.448±0.007	41,43	C1,H	LIH									0.0
Si IV	1.9115	27987	0.439±0.004	0.318±0.004	13,19	C1,H										0.0
								Si IV	1.9118	27949	≤0.248	≤0.197	15,24	C2,H		+30.9
								C IV	1.9119	27946	0.837±0.009	0.679±0.009	47,48	C1,H	LIH	+41.2
C IV	1.9138	27745	0.484±0.009	0.359±0.009	42,44	C3,H										+236.9
Si IV	1.9141	27718	≤0.461	0.205±0.005	15,20	B2,H	LIH									+267.8
Si IV	1.9420	24880	0.041±0.002	0.019±0.003	21,22	C2	LI									
								C IV	2.1081	8460	0.209±0.004	0.110±0.004	51,52	B1,H	IH	0.0
C IV	2.1084	8426	0.130±0.002	0.074±0.002	45,46	C2	IH									+29.0
C IV	2.1196	7348	≤0.065	0.024±0.001	47,48	C2	LH									0.0
								C IV	2.1209	7223	0.552±0.003	0.470±0.003	53,54	C1,H	LIH	+125.0
C IV	2.1270	6643	0.145±0.001	0.114±0.001	49,50	C1	H									0.0
								C IV	2.1276	6585	0.029±0.002	0.014±0.002	55,57	C2	IH	+57.5
								C IV	2.1285	6500	0.183±0.002	0.155±0.002	56,58	C1,H		+143.9
C IV	2.1349	5884	0.093±0.003	0.046±0.002	51,52	C1	H									0.0
								C IV	2.1349	5886	0.073±0.002	0.032±0.002	59,60	C2	H	0.0

TABLE 2
Absorption Systems with Doublet Lines

C IV	2.1800	1604	0.011±0.001	0.008±0.001	53,55	C2	IH								0.0
Si IV	2.1815	1458	0.115±0.006	0.041±0.005	33,34	C1									+141.5
								C IV	2.1818	1428	0.298±0.002	0.209±0.002	61,62	C1,H	LIH	+169.7
C IV	2.1819	1416	0.425±0.004	≤0.297	54,56	C1,H									+179.2
								Si IV	2.1821	1403	0.088±0.002	0.062±0.003	39,40	C1		+198.0
								C IV	2.1897	686	0.848±0.003	≤1.405	63,64	A1,H	H	0.0
C IV	2.1898	676	0.902±0.003	≤1.253	57,58	A1,H	H									+9.4
N V	2.1900	657	0.945±0.004	≤0.882	1, 3	A1,H										+28.2
								N V	2.1900	658	0.888±0.004	≤0.717	1, 3	A1,H		+28.2
N V	2.1955	141	≤1.494	1.341±0.004	2, 4	A1,H	H									0.0
								N V	2.1955	141	≤1.231	1.201±0.003	2, 4	A1,H	H	0.0
								C IV	2.1957	122	1.569±0.003	1.224±0.003	65,66	A1,H		+18.8
C IV	2.1958	113	≤1.590	1.303±0.003	59,60	A1,H										+28.2

[a] Rest-frame equivalent width of blue component of doublet line.
[b] Rest-frame equivalent width of red component of doublet line.
[c] Reliability class of intrinsic lines based on partial coverage analysis, defined in Misawa et al. (2007a). If an equivalent width is large enough, we classify the doublet as *homogeneous* sample with a mark of "H".
[d] Ionization class of absorption system with high (H; IP > 60 eV), intermediate (I; IP = 35 – 50 eV), and/or low (L; IP < 25 eV) ionization transitions.
[e] Velocity difference from the first doublet in each absorption *system*.

TABLE 3
Line Parameters of Narrow Absorption Components

Ion	$\lambda_{\rm obs}$[a] (Å)	$z_{\rm abs}$[b]	$v_{\rm ej}$[c] (km s^{-1})	$\log N$ (cm^{-2})	$\sigma(v)/b$[d] (km s^{-1})	$C_{\rm f}$[e]	Other Ions[f]
			Image A				
Mg II	4225.6	0.5111	190431		47.3		Mg I λ2853, Fe II λ2600 (Fe II λ2383)
		0.5108	190464	12.96±0.06	5.1±0.2	$0.93^{+0.07}_{-0.06}$	
		0.5112	190426	13.51±0.05	10.5±0.5	$1.00^{+0.06}_{-0.06}$	
		0.5112	190423	13.69±0.33	37.1±7.2	$0.19^{+0.10}_{-0.09}$	
		0.5113	190408	12.60±0.02	7.6±0.3	1.00	
Mg II	4229.5	0.5125	190265		17.9		Mg I λ2853, Fe II λ2600 (Fe II λ2344, Fe II λ2383)
		0.5125	190269	12.69±0.02	6.0±0.4	1.00	
		0.5126	190261	12.70±0.27	13.3±4.2	$0.83^{+0.46}_{-0.28}$	
Mg II	5376.1	0.9176	141245		14.1		Mg I λ2853, Fe II λ2600 (Al III λ1863)
		0.9176	141246	12.95±0.02	4.7±0.2	1.00	
Mg II	5365.3	0.9187	141116		68.1		Mg I λ2853, Fe II λ2344,2600 (Al III λ1863)
		0.9181	141190	12.50±0.02	4.1±0.3	1.00	
		0.9185	141146	14.03±0.02	16.9±0.2	1.00	
		0.9189	141094	14.94±0.07	22.0±0.5	$0.99^{+0.03}_{-0.03}$	
C IV	4048.7	1.6151	59472		26.0		Si IV λ1394,1403
		1.6151	59473	17.33±0.06	8.7±0.1	$1.00^{+0.04}_{-0.04}$	
C IV	4050.1	1.6160	59378		13.1		
		1.6160	59379	13.66±0.15	10.3±1.1	$0.42^{+0.08}_{-0.08}$	
C IV	4067.7	1.6230	58601		38.3		
		1.6229	58617	13.84±0.02	13.0±0.8	1.00	
		1.6231	58590	13.93±0.06	5.4±0.6	1.00	
		1.6236	58538	12.88±0.09	9.7±3.0	1.00	
C IV	4169.3	1.6930	50965		58.4		Si II λ1527, Al II λ1671 (O I λ1302, Si II λ1260, C II λ1335, Si IV λ1394)
		1.6928	50991	13.69±0.02	39.0±1.8	1.00	
		1.6934	50925	13.52±0.02	17.9±0.7	1.00	
C IV	4212.9	1.7212	47932		41.9		Lyα
		1.7209	47955	13.25±0.02	11.1±0.7	1.00	
		1.7214	47908	13.16±0.02	9.2±0.7	1.00	
C IV	4281.1	1.7652	43224		10.0		Lyα(O I λ1302, Si II λ1207, Si IV λ1394)
		1.7652	43223	13.71±0.11	6.1±0.5	$0.58^{+0.06}_{-0.06}$	
C IV	4475.7	1.8909	30091		30.8		Lyα, Si II λ1527, Al II λ1671, (Si II λ1190,1192,1260, C II λ1335, Si III λ1207)
		1.8909	30090	14.83±0.05	20.9±0.5	$0.96^{+0.05}_{-0.05}$	
Si IV	4029.3	1.8909	30088		27.1		Lyα, Si II λ1527, Al II λ1671, (Si II λ1190,1192,1260, C II λ1335, Si III λ1207)
		1.8906	30121	12.48±0.11	2.8±0.9	1.00	
		1.8907	30111	12.49±0.14	8.8±3.1	1.00	
		1.8910	30081	13.56±0.02	11.2±0.4	1.00	
C IV	4481.8	1.8949	29686		36.5		Lyα(C II λ1335, Si III λ1207, N V λ1239,1243)
		1.8945	29728	12.85±0.26	7.7±3.0	1.00	

TABLE 3
Line Parameters of Narrow Absorption Components

		1.8947	29703	14.14±0.22	12.5±4.2	1.00	
		1.8949	29684	14.57±0.23	9.0±1.3	1.00	
		1.8952	29654	13.74±0.02	8.7±0.4	1.00	
Si IV	4034.7	1.8949	29685		38.2		Lyα(C II λ1335, Si III λ1207, N V λ1239,1243)
		1.8949	29684	16.17±0.05	2.2±0.4	1.00	
C IV	4487.0	1.8982	29343		22.5		Lyα
		1.8981	29353	13.87±0.07	11.9±1.0	$0.88^{+0.07}_{-0.07}$	
		1.8983	29332	13.45±0.02	12.8±0.6	1.00	
Si IV	4039.4	1.8982	29342		19.9		Lyα
		1.8980	29360	11.95±0.09	4.8±1.6	1.00	
		1.8983	29337	12.40±0.04	9.3±1.2	1.00	
C IV	4507.6	1.9115	27981		48.8		Lyα, Si II λ1527, Al II λ1671 (O I λ1302, Si II λ1190,1193,1260, Si III λ1207)
		1.9115	27984	14.79±0.04	36.0±0.9	$0.98^{+0.08}_{-0.08}$	
Si IV	4057.9	1.9115	27987		44.5		Lyα, Si II λ1527, Al II λ1671 (O I λ1302, Si II λ1190,1193,1260, Si III λ1207)
		1.9112	28017	13.43±0.04	13.7±1.2	1.00	
		1.9114	27995	13.35±0.04	7.5±0.7	1.00	
		1.9115	27979	13.46±0.03	46.9±2.4	1.00	
		1.9116	27973	13.84±0.07	12.3±1.4	$0.96^{+0.06}_{-0.06}$	
C IV	4511.2	1.9138	27745		64.0		Lyα, Si II λ1527, Al II λ1671, C II λ1335 (Si II λ1190,1193,1260, Si III λ1207, N V λ1239,1243)
		1.9133	27797	14.10±0.08	23.1±1.4	$0.69^{+0.09}_{-0.08}$	
		1.9141	27716	14.34±0.02	21.2±0.6	1.00	
Si IV	4087.8	1.9141	27718		17.2		Lyα, Si II λ1527, Al II λ1671, C II λ1335 (Si II λ1190,1193,1260, Si III λ1207, N V λ1239,1243)
		1.9141	27720	13.61±0.02	10.9±0.4	1.00	
		1.9143	27694	12.38±0.09	4.9±1.7	1.00	
Si IV	4100.4	1.9420	24880		13.2		Lyα, Si II λ1527, Al II λ1671, C II λ1335 (O I λ1302, Si II λ1190,1193,1260, Si III λ1207)
		1.9420	24879	12.70±0.02	10.2±0.7	1.00	
C IV	4812.5	2.1084	8426		21.2		Lyα, Si IV λ1394 (Si III λ1207)
		2.1083	8435	13.46±0.03	11.8±0.7	1.00	
		2.1086	8415	13.19±0.06	10.8±1.0	1.00	
C IV	4829.8	2.1196	7348		17.1		Lyα, C II λ1335
		2.1196	7349	13.63±0.14	13.9±1.0	$0.43^{+0.12}_{-0.09}$	
C IV	4841.2	2.1270	6643		16.4		Lyα(N V λ1239,1243)
		2.1270	6644	13.68±0.10	14.5±0.6	$0.90^{+0.12}_{-0.12}$	
		2.1270	6638	13.86±0.02	5.2±0.1	1.00	
C IV	4853.4	2.1349	5884		35.3		Lyα
		2.1347	5903	13.03±0.02	20.9±1.5	1.00	
		2.1351	5866	13.34±0.18	11.3±0.8	$0.70^{+0.45}_{-0.24}$	
C IV	4923.2	2.1800	1604		14.3		Lyα
		2.1799	1606	13.48±0.35	10.2±2.3	$0.15^{+\infty}_{-0.08}$	
Si IV	4434.2	2.1815	1458		73.3		Lyα(Si III λ1207)
		2.1810	1502	12.72±0.03	5.8±0.8	1.00	

TABLE 3
Line Parameters of Narrow Absorption Components

		2.1818	1427	12.54±0.07	19.5±4.4	1.00	
		2.1822	1395	12.94±0.25	3.0±1.1	$0.72^{+0.23}_{-0.23}$	
C IV	4926.3	2.1819	1416		34.0		Lyα(Si III λ1207)
		2.1817	1436	13.69±0.09	16.5±1.7	$0.88^{+0.10}_{-0.10}$	
		2.1820	1409	13.89±0.01	29.1±0.3	1.00	
		2.1822	1394	13.61±0.01	6.0±0.3	1.00	
C IV[g]	4944.5	2.1937	347		400.1		Lyα, Si IV λ1394, O VI λ1032,1038
		2.1881	878	13.24±0.01	25.6±0.8	1.00	
		2.1886	831	14.49±0.07	11.6±0.6	$0.43^{+0.02}_{-0.02}$	
		2.1889	795	14.27±0.23	8.6±1.3	$0.38^{+0.02}_{-0.02}$	
		2.1892	773	13.77±0.20	11.1±1.4	$0.52^{+0.08}_{-0.08}$	
		2.1894	748	14.30±0.17	7.8±1.0	$0.44^{+0.02}_{-0.02}$	
		2.1900	693	14.49±0.02	25.3±0.6	$0.84^{+0.02}_{-0.02}$	
		2.1909	613	14.04±0.03	20.3±0.5	$0.98^{+0.03}_{-0.03}$	
		2.1914	567	13.31±0.01	16.6±0.3	1.00	
		2.1943	287	14.53±0.02	17.8±0.2	$0.91^{+0.02}_{-0.02}$	
		2.1947	254	14.84±0.18	10.0±1.0	$0.52^{+0.02}_{-0.02}$	
		2.1953	201	14.63±0.02	22.5±0.7	$0.89^{+0.02}_{-0.02}$	
		2.1961	124	14.88±0.03	29.4±0.9	$0.81^{+0.02}_{-0.02}$	
		2.1968	61	14.48±0.02	25.9±0.6	$0.84^{+0.02}_{-0.02}$	
		2.1975	−11	14.28±0.02	19.6±0.5	$0.46^{+0.02}_{-0.02}$	
		2.1981	−63	13.91±0.03	14.9±0.6	$0.47^{+0.03}_{-0.03}$	
		2.1985	−100	14.09±0.09	11.5±1.0	$0.18^{+0.02}_{-0.02}$	
N V[h]	3956.5	2.1937	343		428.4		Lyα, Si IV λ1394, O VI λ1032,1038
		2.1879	889	13.38±0.02	23.8±1.2	1.00	
		2.1885	834	13.81±0.13	17.4±1.0	$0.85^{+0.18}_{-0.17}$	
		2.1893	762	14.26±0.04	42.5±1.7	$0.97^{+0.06}_{-0.06}$	
		2.1900	691	14.88±0.03	20.6±0.5	$0.88^{+0.03}_{-0.03}$	
		2.1909	614	14.55±0.02	23.5±0.5	$0.97^{+0.03}_{-0.03}$	
		2.1914	567	13.90±0.01	15.0±0.2	1.00	
		2.1944	285	14.83±0.02	22.1±0.4	$0.97^{+0.03}_{-0.03}$	
		2.1953	201	14.92±0.01	41.1±1.6	$0.97^{+0.03}_{-0.03}$	
		2.1961	125	15.45±0.33	14.9±1.8	$0.84^{+0.04}_{-0.04}$	
		2.1966	75	15.21±0.05	26.7±0.8	$0.92^{+0.03}_{-0.03}$	
		2.1976	−14	14.38±0.04	25.6±1.4	$0.62^{+0.03}_{-0.03}$	
		2.1981	−61	14.21±0.09	10.9±1.2	$0.53^{+0.06}_{-0.06}$	
		2.1984	−91	13.66±0.01	26.3±0.7	1.00	
Image B							
Mg II	4229.3	0.5124	190276		11.7		Fe II λ2600
		0.5124	190275	12.68±0.18	11.3±0.9	$0.69^{+0.29}_{-0.20}$	
Mg II	4678.6	0.6731	171003		78.2		Mg I λ2853, Fe II λ2344,2383,2600
		0.6725	171070	13.02±1.03	2.4±1.9	$0.31^{+0.10}_{-0.09}$	
		0.6726	171059	13.49±0.14	7.5±1.7	$0.92^{+0.08}_{-0.08}$	

TABLE 3
Line Parameters of Narrow Absorption Components

		0.6727	171047	12.83±0.52	16.5±18.7	$1.00^{+0.21}_{-0.18}$	
		0.6729	171032	13.03±0.24	8.1±2.4	$1.00^{+0.06}_{-0.06}$	
		0.6730	171018	13.27±0.01	12.0±0.3	1.00	
		0.6731	171008	14.29±9.79	3.2±9.0	$0.98^{+0.06}_{-0.06}$	
		0.6732	170994	13.29±0.01	16.5±0.4	1.00	
		0.6733	170980	13.67±0.16	20.7±5.0	$1.00^{+0.05}_{-0.05}$	
		0.6735	170955	13.29±0.01	17.6±0.3	1.00	
		0.6736	170947	13.38±0.44	6.0±2.0	$0.55^{+0.14}_{-0.14}$	
Mg II	5364.4	0.9184	141157		33.1		
		0.9181	141186	12.45±0.59	9.1±2.0	$0.29^{+\infty}_{-0.32}$	
		0.9184	141158	12.65±0.12	9.6±1.0	$0.68^{+0.18}_{-0.13}$	
		0.9185	141142	12.22±0.02	11.8±0.7	1.00	
C IV	4038.4	1.6085	60206		11.2		
		1.6085	60206	13.57±0.18	8.0±0.9	$0.44^{+0.10}_{-0.10}$	
C IV	4048.4	1.6149	59493		20.6		(Si IV λ1394,1403)
		1.6150	59491	12.38±0.08	2.5±4.5	1.00	
		1.6150	59487	14.04±0.06	9.2±0.4	$0.71^{+0.06}_{-0.06}$	
C IV	4066.3	1.6221	58699		19.0		
		1.6222	58699	14.12±0.02	13.4±0.4	1.00	
C IV	4064.5	1.6253	58350		13.7		
		1.6253	58348	13.57±0.24	6.0±0.9	$0.28^{+0.08}_{-0.08}$	
C IV	4111.4	1.6556	55033		22.1		
		1.6556	55033	13.82±0.06	14.7±0.5	$0.85^{+0.07}_{-0.06}$	
C IV	4168.4	1.6924	51029		14.7		
		1.6925	51027	13.42±0.01	11.4±0.5	1.00	
C IV	4190.2	1.7065	49509		11.7		
		1.7065	49508	13.68±0.14	7.8±0.8	$0.46^{+0.07}_{-0.06}$	
C IV	4275.7	1.7617	43596		11.1		Lyα
		1.7617	43596	14.17±9.99	4.5±25.6	$0.15^{+0.11}_{-0.11}$	
C IV	4277.1	1.7627	43496		20.9		Lyα, Si II λ1527 (Si II λ1260, C II λ1335, Si III λ1207, Si IV λ1394,1403)
		1.7626	43503	13.78±0.07	7.6±0.7	$0.83^{+0.07}_{-0.06}$	
		1.7628	43479	13.92±0.37	22.0±16.2	$0.17^{+\infty}_{-0.07}$	
C IV	4280.7	1.7650	43250		15.8		Lyα
		1.7650	43249	13.64±0.20	11.7±1.4	$0.36^{+0.12}_{-0.10}$	
C IV	4475.7	1.8909	30088		48.6		Lyα(Si III λ1207)
		1.8904	30140	13.42±0.03	11.4±0.8	1.00	
		1.8910	30084	14.31±0.06	25.0±2.3	1.00	
		1.8913	30055	13.15±0.59	10.4±6.0	1.00	
		1.8915	30027	13.00±0.08	11.3±2.2	1.00	
Si IV[i]	4029.3	1.8909	30087		38.2		Lyα(Si III λ1207)

TABLE 3
Line Parameters of Narrow Absorption Components

Si IV	4034.0	1.8944	29737		76.4		Lyα, Si II λ1527, Al II λ1671 (Si II λ1190,1193,1260, C II λ1335, Si III λ1207)
		1.8940	29771	13.87±0.02	22.5±0.4	1.00	
		1.8947	29700	12.33±0.08	10.1±2.1	1.00	
		1.8950	29675	12.92±0.02	11.3±0.7	1.00	
		1.8954	29629	12.70±0.03	12.6±0.9	1.00	
C IV	4488.7	1.8945	29723		75.2		Lyα, Si II λ1527, Al II λ1671 (Si II λ1190,1193,1260, C II λ1335, Si III λ1207)
		1.8939	29785	14.14±0.09	16.9±1.9	1.00	
		1.8942	29753	14.51±0.05	18.7±1.4	1.00	
		1.8946	29708	13.23±0.14	7.7±1.7	1.00	
		1.8949	29682	14.25±0.03	16.6±1.2	1.00	
		1.8953	29638	13.76±0.07	31.2±5.3	1.00	
Si IV	4038.4	1.8975	29413		11.2		Lyα, C IV λ1548,1551 (Si II λ1260, Si III λ1207)
		1.8975	29414	13.07±0.20	7.4±0.9	$0.50^{+0.16}_{-0.13}$	
Si IV	4044.2	1.9016	28991		18.5		Lyα, Si II λ1527, Al II λ1671 (Si II λ1190,1193,1260, C II λ1335, Si III λ1207)
		1.9016	28992	13.87±0.04	12.8±0.3	$0.92^{+0.05}_{-0.05}$	
C IV	4492.7	1.9019	28964		52.4		Lyα, Si II λ1527, Al II λ1671 (Si II λ1190,1193,1260, C II λ1335, Si III λ1207)
		1.9017	28988	14.51±0.03	21.6±0.5	$0.96^{+0.07}_{-0.07}$	
		1.9024	28918	13.87±0.05	12.5±0.4	$0.97^{+0.08}_{-0.07}$	
Si IV	4045.2	1.9024	28917		11.1		Lyα, C IV λ1548,1551
		1.9023	28918	13.19±0.25	6.8±1.2	$0.31^{+0.10}_{-0.09}$	
Si IV	4058.4	1.9118	27949		26.7		Lyα, Si II λ1527, Al II λ1671 (O I λ1302, Si II λ1190,1193,1260, Si III λ1207)
		1.9117	27964	13.38±0.01	13.5±0.2	1.00	
		1.9120	27933	13.67±0.04	18.0±1.9	$0.96^{+0.04}_{-0.04}$	
C IV	4508.1	1.9119	27946		88.7		Lyα, Si II λ1527, Al II λ1671 (O I λ1302, Si II λ1190,1193,1260, Si III λ1207)
		1.9110	28034	13.73±0.02	34.6±1.8	1.00	
		1.9121	27921	15.09±0.04	38.3±0.9	$0.98^{+0.09}_{-0.09}$	
C IV	4811.9	2.1081	8460		62.0		Lyα, Si IV λ1394,1403 (Si III λ1207)
		2.1076	8508	13.12±0.02	28.8±1.9	1.00	
		2.1078	8486	13.27±0.21	8.3±1.1	$0.70^{+0.46}_{-0.25}$	
		2.1084	8432	13.06±0.02	15.7±0.9	1.00	
		2.1085	8416	13.64±0.07	9.0±1.0	$0.70^{+0.09}_{-0.09}$	
C IV	4831.8	2.1209	7223		55.1		Lyα, O I λ1302Si II λ1260, C II λ1335, Si IV λ1394,1403 (Si II λ1207)
		2.1205	7261	14.42±0.03	14.3±0.4	$0.96^{+0.04}_{-0.04}$	
		2.1209	7225	14.04±0.03	10.1±0.4	$0.92^{+0.04}_{-0.04}$	
		2.1214	7180	14.35±0.02	13.2±0.2	1.00	
C IV	4842.1	2.1276	6585		22.9		Lyα
		2.1276	6588	12.93±0.03	15.0±1.5	1.00	
C IV	4843.5	2.1285	6500		19.4		Lyα, Si IV λ1394,1403
		2.1285	6500	14.22±0.02	12.8±0.2	$0.97^{+0.04}_{-0.04}$	
C IV	4853.4	2.1349	5886		32.8		Lyα
		2.1346	5913	12.83±0.03	10.1±0.8	1.00	

TABLE 3
Line Parameters of Narrow Absorption Components

		2.1350	5871	13.12±0.02	20.4±1.2	1.00	
C IV	4926.1	2.1818	1428		48.5		Lyα, Si II λ1260, Si IV λ1394,1403 (Si II λ1193, Si III λ1207)
		2.1810	1503	12.66±0.08	16.1±3.4	1.00	
		2.1814	1471	13.30±0.02	13.9±0.5	1.00	
		2.1818	1431	12.91±0.02	13.3±0.6	1.00	
		2.1821	1406	14.17±0.01	14.1±0.2	$0.97^{+0.03}_{-0.03}$	
Si IV	4435.0	2.1821	1403		12.1		Lyα, Si II λ1260, Si IV λ1394,1403 (Si II λ1193, Si III λ1207)
		2.1820	1411	13.69±0.31	5.2±1.3	$0.38^{+0.07}_{-0.07}$	
		2.1821	1399	13.16±0.11	7.2±0.6	$0.77^{+0.10}_{-0.10}$	
C IV[j]	4944.5	2.1937	348		393.5		Lyα, Si II λ1260, Si IV λ1394,1403 (Si II λ1193, Si III λ1207)
		2.1885	840	14.45±0.07	39.5±3.5	$0.22^{+0.02}_{-0.02}$	
		2.1896	735	14.45±0.06	45.5±3.0	$0.73^{+0.03}_{-0.03}$	
		2.1901	689	14.27±0.06	23.1±1.5	$0.62^{+0.08}_{-0.08}$	
		2.1909	614	13.94±0.05	18.4±0.8	$0.91^{+0.05}_{-0.05}$	
		2.1913	573	13.85±0.39	29.2±2.6	$0.44^{+0.23}_{-0.23}$	
		2.1943	288	14.50±0.01	22.7±0.3	$0.93^{+0.02}_{-0.02}$	
		2.1949	231	15.90±0.64	13.5±2.3	$0.38^{+0.02}_{-0.02}$	
		2.1952	204	14.48±0.05	17.4±0.9	$0.80^{+0.03}_{-0.03}$	
		2.1956	167	14.18±0.05	11.3±1.0	$0.67^{+0.05}_{-0.05}$	
		2.1961	120	14.69±0.02	29.5±2.0	$0.83^{+0.02}_{-0.02}$	
		2.1966	80	14.22±0.28	7.6±1.7	$0.39^{+0.08}_{-0.08}$	
		2.1968	57	14.19±0.04	17.1±1.4	$0.66^{+0.05}_{-0.05}$	
		2.1970	35	14.19±0.04	25.5±1.5	$0.62^{+0.04}_{-0.03}$	
		2.1977	−25	14.58±0.04	45.6±2.2	$0.23^{+0.02}_{-0.02}$	
N V[k]	3956.2	2.1935	364		402.7		Lyα, Si II λ1260, Si IV λ1394,1403 (Si II λ1193, Si III λ1207)
		2.1879	896	14.45±1.01	13.4±9.3	$0.04^{+0.03}_{-0.03}$	
		2.1883	857	13.11±0.03	9.3±1.7	1.00	
		2.1893	759	14.02±0.15	15.8±1.9	$0.64^{+0.14}_{-0.14}$	
		2.1895	745	14.60±0.07	66.5±3.9	$0.79^{+0.07}_{-0.07}$	
		2.1899	701	14.89±0.06	25.5±2.0	$0.75^{+0.05}_{-0.05}$	
		2.1909	613	14.48±0.02	19.6±0.6	$0.94^{+0.03}_{-0.03}$	
		2.1914	566	13.90±0.01	17.9±0.4	1.00	
		2.1944	282	14.85±0.02	31.1±0.5	$0.96^{+0.03}_{-0.03}$	
		2.1952	209	14.53±0.26	9.5±1.5	$0.79^{+0.05}_{-0.05}$	
		2.1954	193	15.45±0.13	24.5±1.7	$0.81^{+0.03}_{-0.03}$	
		2.1965	86	15.26±0.02	51.6±1.0	$0.94^{+0.03}_{-0.03}$	
		2.1980	−53	14.16±0.13	29.5±2.2	$0.39^{+0.08}_{-0.08}$	

TABLE 3
Line Parameters of Narrow Absorption Components

[a] Wavelength of flux-weighted line center.
[b] Redshift of flux weighted line center.
[c] Ejection velocity from quasar emission redshift.
[d] Flux-weighted line width ($\sigma(v)$) or Doppler parameter (b).
[e] Covering factor.
[f] Other single lines that are detected in the system. Lines in parenthesis are in Lyα forest.
[g] Two C IV PALs at $z_{\rm abs} \sim 2.1898$ and 2.1958 are fitted together as a single absorption profile whose flux-weighted redshift is $z_{\rm abs} \sim 2.1937$.
[h] Two N V PALs at $z_{\rm abs} \sim 2.1900$ and 2.1955 are fitted together as a single absorption profile whose flux-weighted redshift is $z_{\rm abs} \sim 2.1937$.
[i] We cannot fit this Si IV NAL because both members of the doublet are blending with other lines.
[j] Two C IV PALs at $z_{\rm abs} \sim 2.1897$ and 2.1957 are fitted together as a single absorption profile whose flux-weighted redshift is $z_{\rm abs} \sim 2.1937$.
[k] Two N V PALs at $z_{\rm abs} \sim 2.1900$ and 2.1955 are fitted together as a single absorption profile whose flux-weighted redshift is $z_{\rm abs} \sim 2.1935$.

TABLE 4
Statistical Properties of Poisson Systems of NALs

		C IV			N V			Si IV		
		AAL[a]	non-AAL[b]	total	AAL[a]	non-AAL[b]	total	AAL[a]	non-AAL[b]	total
Path length	δz[c]	0.05	0.56	0.61	0.05	0.01	0.07	0.05	0.37	0.42
	$\delta\beta$[c]	0.02	0.19	0.21	0.02	0.00	0.02	0.02	0.12	0.14
Image A	N^d	$3^{+2.9}_{-1.6}$	$9^{+4.1}_{-2.9}$	$12^{+4.6}_{-3.4}$	$2^{+2.6}_{-1.3}$	$0^{+1.8}_{-0}$	$2^{+2.6}_{-1.3}$	$0^{+1.8}_{-0}$	$3^{+2.9}_{-1.6}$	$3^{+2.9}_{-1.6}$
	dN/dz	57^{+55}_{-31}	$16^{+7.3}_{-5.3}$	$20^{+7.4}_{-5.6}$	38^{+50}_{-24}	0^{+132}_{-0}	30^{+39}_{-19}	0^{+35}_{-0}	$8.1^{+7.9}_{-4.4}$	$7.1^{+6.9}_{-3.9}$
	$dN/d\beta$	177^{+172}_{-96}	47^{+22}_{-16}	58^{+22}_{-17}	118^{+155}_{-76}	0^{+409}_{-0}	93^{+123}_{-60}	0^{+108}_{-0}	25^{+24}_{-14}	22^{+21}_{-12}
Image B	N^d	$3^{+2.9}_{-1.6}$	$8^{+4.0}_{-2.8}$	$11^{+4.4}_{-3.3}$	$2^{+2.6}_{-1.3}$	$0^{+1.8}_{-0}$	$2^{+2.6}_{-1.3}$	$0^{+1.8}_{-0}$	$3^{+2.9}_{-1.6}$	$3^{+2.9}_{-1.6}$
	dN/dz	57^{+55}_{-31}	$14^{+7.1}_{-4.9}$	$18^{+7.2}_{-5.3}$	38^{+50}_{-24}	0^{+132}_{-0}	30^{+39}_{-19}	0^{+35}_{-0}	$8.1^{+7.9}_{-4.4}$	$7.1^{+6.9}_{-3.9}$
	$dN/d\beta$	177^{+172}_{-96}	42^{+21}_{-15}	53^{+21}_{-16}	118^{+155}_{-76}	0^{+409}_{-0}	93^{+123}_{-60}	0^{+108}_{-0}	25^{+24}_{-14}	22^{+21}_{-12}
M07a[e]	dN/dz	14.	6.6	6.9	5.2	0.0	4.6	3.2	3.7	3.7
	$dN/d\beta$	54.	24.	25.	21.	0.0	18.	13.	14.	14.

[a] Associated absorption lines with $v_{\rm ej} \leq 5000$ km s^{-1} from the quasar emission redshift.
[b] Non-associated absorption lines with $v_{\rm ej} > 5000$ km s^{-1} from the quasar emission redshift.
[c] Total redshift and speed intervals considered in the determination of dN/dz and $dN/d\beta$.
[d] Number of Poisson systems (i.e., groups of NALs that lie within 200 km s^{-1} of each other).
[e] dN/dz and $dN/d\beta$ values from Misawa et al. (2007a).

TABLE 5
Properties of PALs and intrinsic NALs

	PAL[a] (broad)	PAL[b] (narrow)	NAL	reference[c]
Absorber's Transverse Size[d]	$\geq$ rθ	$\leq$ rθ	$\leq$ rθ	1
Ionization Condition[e]	high	high	low – high	1, 2, 3
Radial Velocity[f] ($v_{\rm ej}$)	small	small	large	1
Rotational Velocity[g] ($v_{\rm rot}$)	large	large	small	7, 8, 9
Variability	frequently	frequently	very rare[h]	4, 5, 6
Origin of Variability	ionization condition	gas motion	gas motion (if any)	5
Covering Factor ($C_{\rm f}$)	~ 1	< 1	< 1	1
Background flux source	BELR	BELR	continuum source	1

[a] PALs at $v_{\rm ej} > 0$ km s^{-1} with common absorption profiles in both sightlines.
[b] PALs at $v_{\rm ej} < 0$ km s^{-1} with sightline variation.
[c] References. (1) This paper, (2) Misawa et al. (2007a), (3) Ganguly et al. (2013) (4) Wise et al. (2004), (5) Misawa et al. (2014a), (6) Chen et al. (2015), (7) Murray et al. (1995), (8) Misawa et al. (2005), (9) Hall et al. (2011)
[d] This depends on whether sightline difference is observed (i.e., $\leq$ rθ) or not (i.e., $\geq$ rθ).
[e] Low, intermediate, and high ionization transitions are defined in Section 4.1.3.
[f] Ejection velocity assuming $z_{\rm em} = 2.197$.
[g] Absorbers with small orbital radius tend to have larger rotational velocity (see Section 5.3).
[h] Variation probability is very low for high ejection velocity NALs (Chen et al. 2015), although we confirmed this trend only for a few strong C IV NALs.

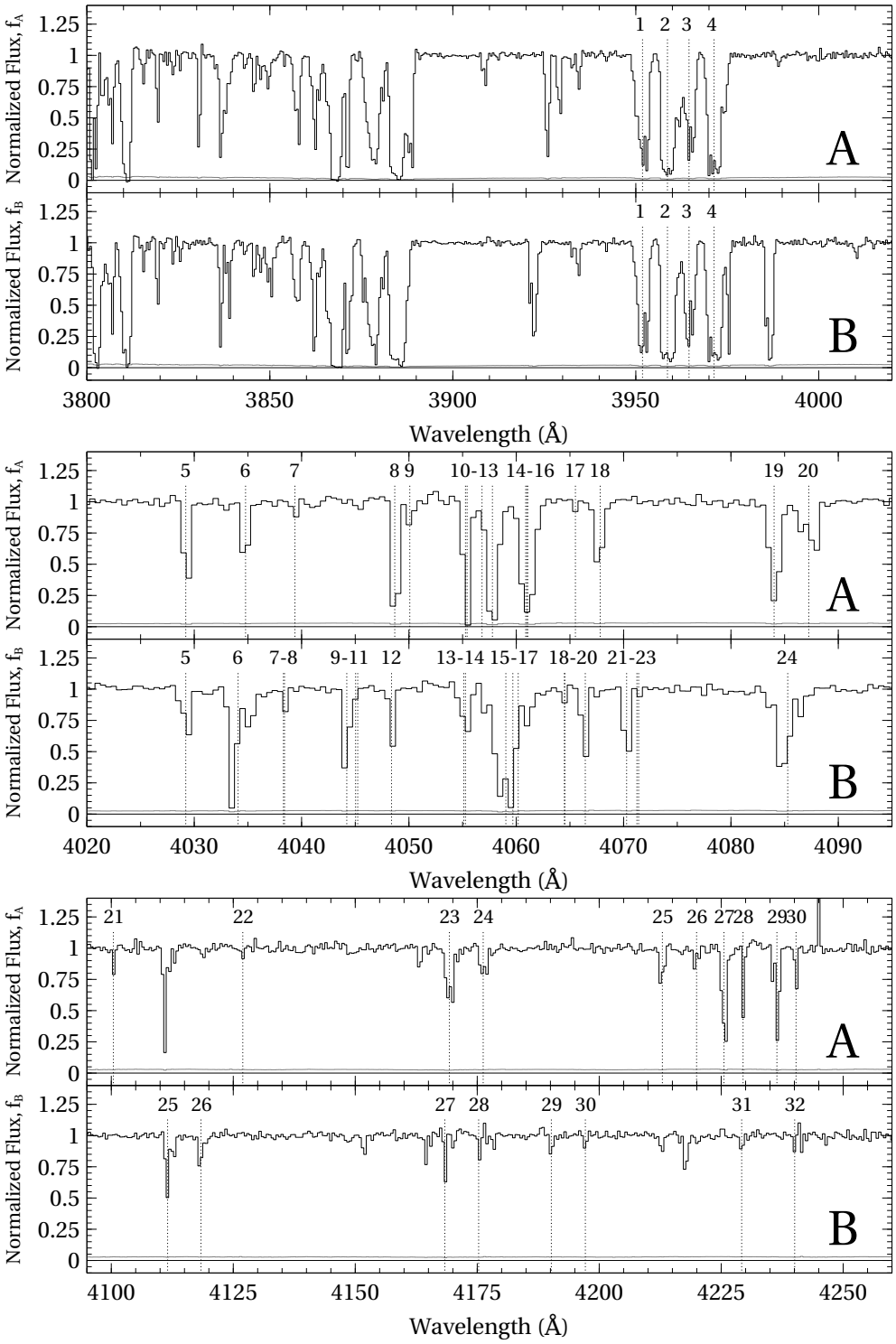

FIG. 1.— Normalized spectra and their 1σ errors for images A and B of SDSS J1029+2623, taken with VLT/UVES, after sampling every 0.5Å for display purpose only.

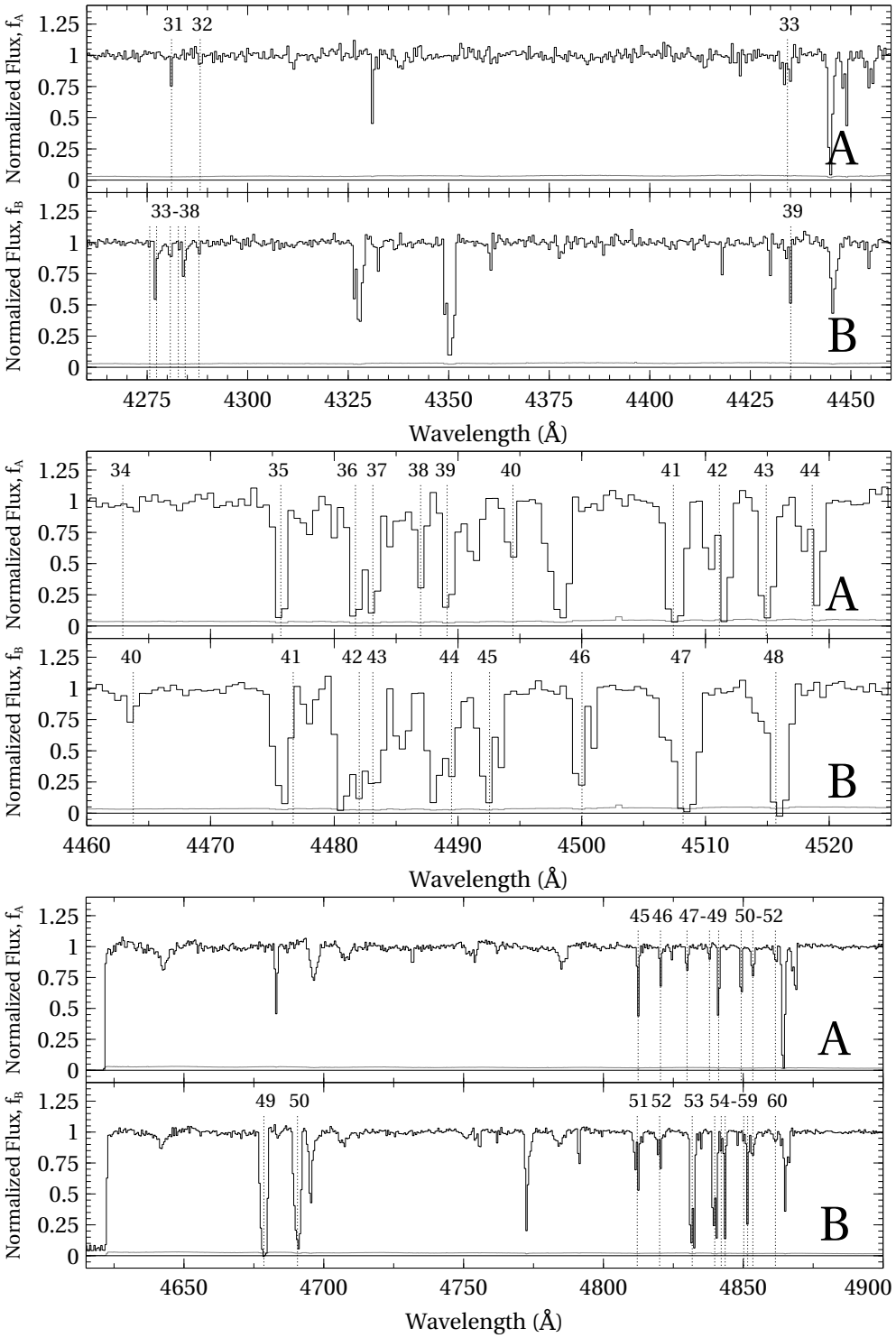

FIG. 1.— Continued.

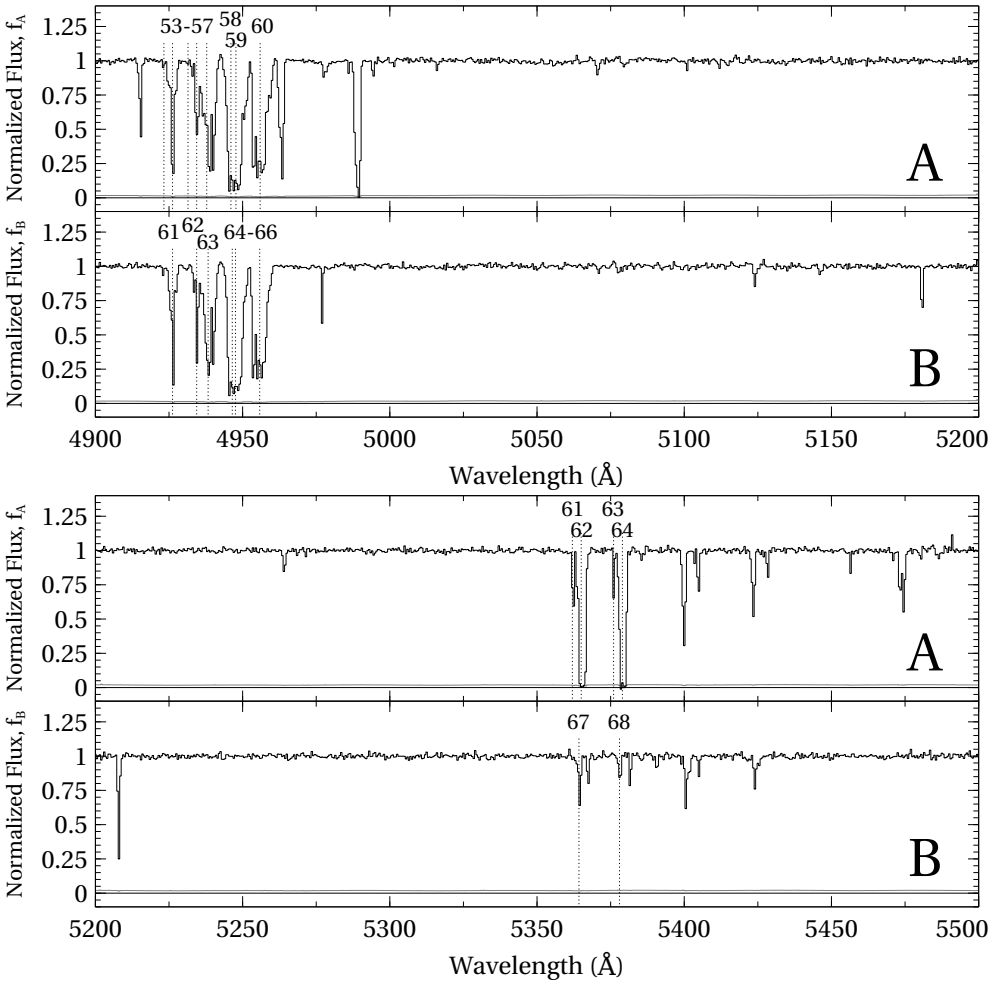

FIG. 1.— Continued.

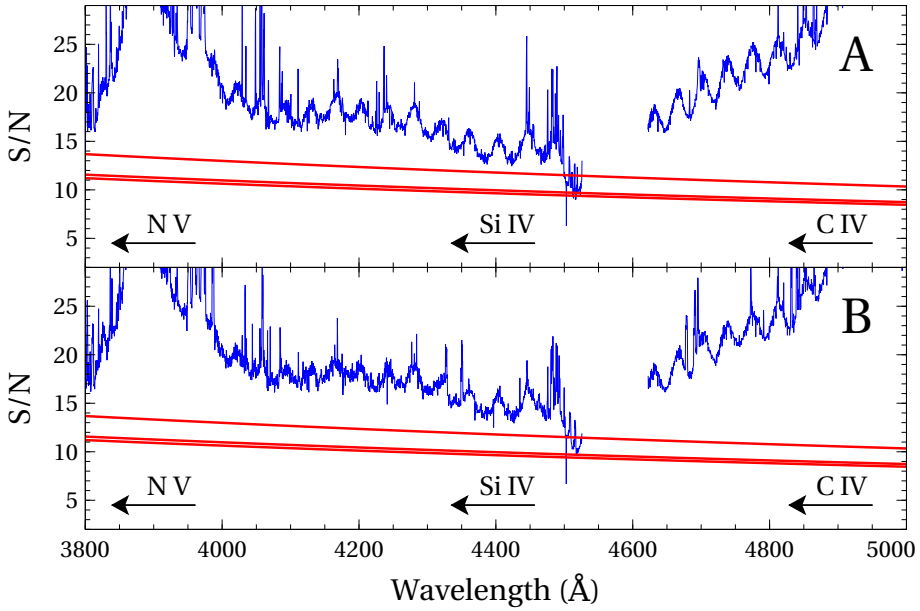

FIG. 2.— Signal-to-Noise (S/N) ratio of the image A and B spectra (blue histograms) and the minimum S/N ratio that is necessary for detecting homogeneous sample lines for N V, C IV, and Si IV, respectively (red lines from top to bottom; see Section 3.1).

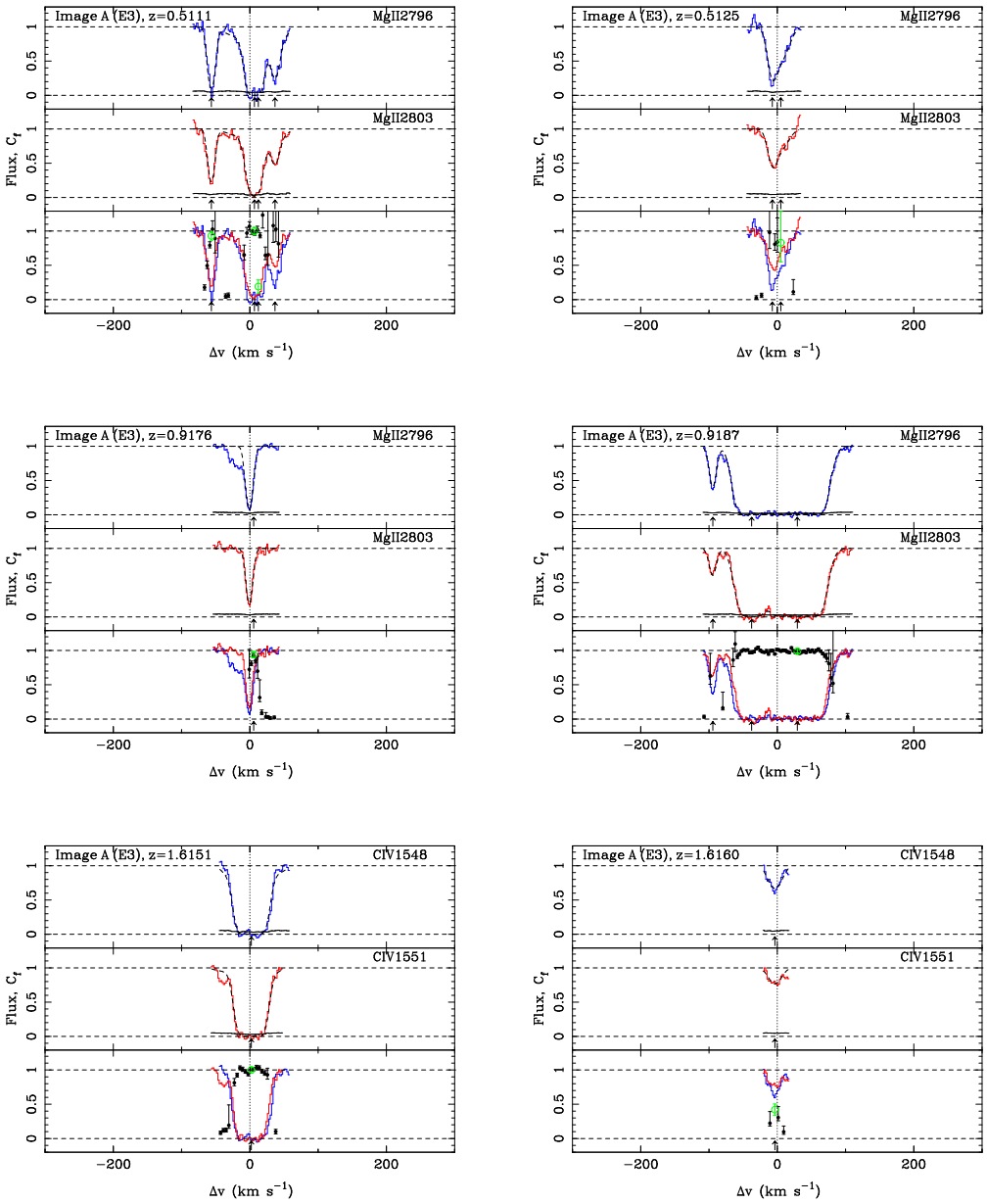

FIG. 3.— Results of partial coverage analysis applied to all C IV, N V, Si IV, and Mg II NALs detected in images A and B of SDSS J1029+2623, except for the PALs whose results are presented in Figure 12. The horizontal axis denotes the relative velocity from the flux-weighted center of the system (Δv) while the vertical axis is the normalized flux. The first two panels show the profiles of the blue and red members of a doublet (blue and red histograms) with the model profile produced by MINFIT superposed (dashed line). The positions of the narrow components are marked with upward arrows in the bottom of each panel. The bottom panel shows the covering factors with their 1σ error bars, measured for each narrow component by MINFIT (green circles) or for each pixel (black dots). If we had to assume $C_f = 1$ for some components because of unphysical C_f values derived from MINFIT (see Section 3.2), we do not plot them.

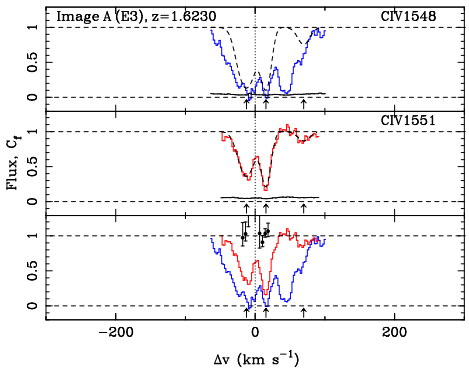
Image A (E3), z=1.6230
CIV1548
CIV1551
Flux, C_f
Δv (km s^{-1})

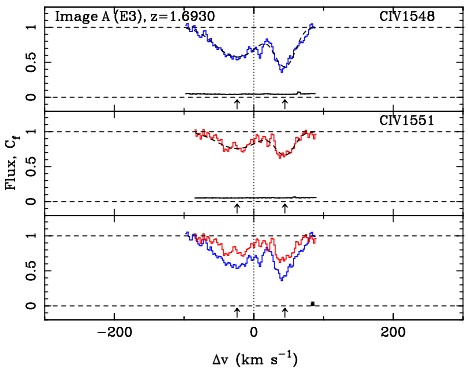
Image A (E3), z=1.6930
CIV1548
CIV1551
Flux, C_f
Δv (km s^{-1})

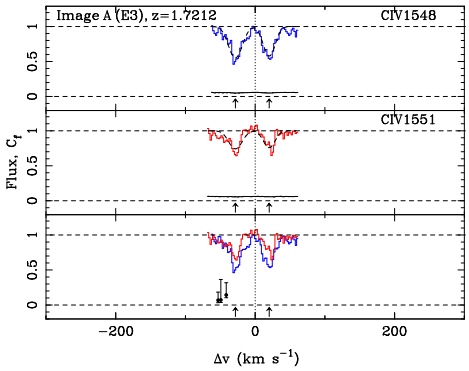
Image A (E3), z=1.7212
CIV1548
CIV1551
Flux, C_f
Δv (km s^{-1})

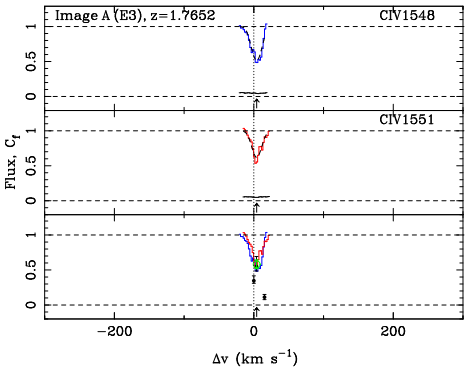
Image A (E3), z=1.7652
CIV1548
CIV1551
Flux, C_f
Δv (km s^{-1})

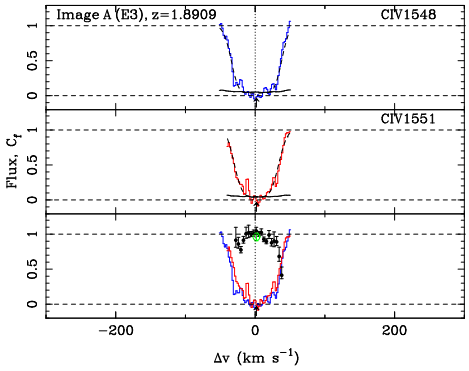
Image A (E3), z=1.8909
CIV1548
CIV1551
Flux, C_f
Δv (km s^{-1})

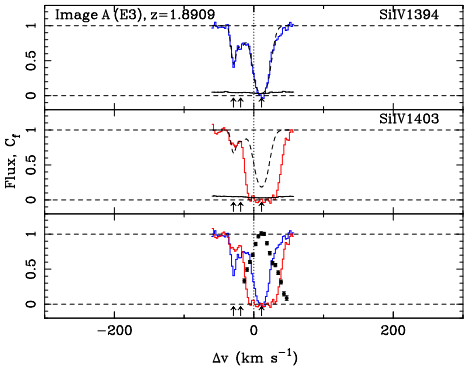
Image A (E3), z=1.8909
SiIV1394
SiIV1403
Flux, C_f
Δv (km s^{-1})

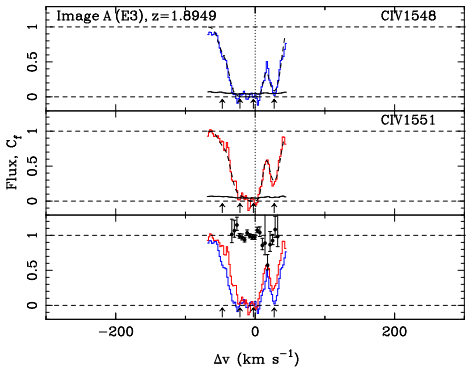
Image A (E3), z=1.8949
CIV1548
CIV1551
Flux, C_f
Δv (km s^{-1})

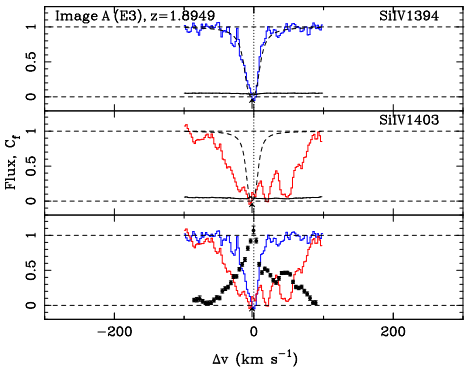
Image A (E3), z=1.8949
SiIV1394
SiIV1403
Flux, C_f
Δv (km s^{-1})

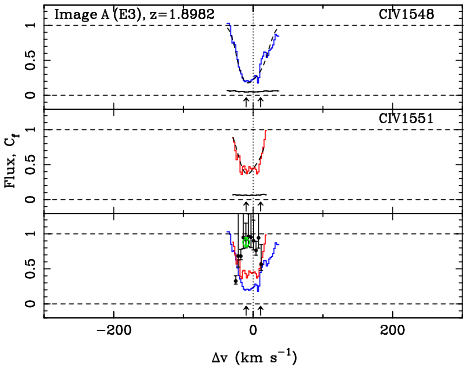
Image A (E3), z=1.8982
CIV1548
CIV1551
Flux, C_f
Δv (km s^{-1})

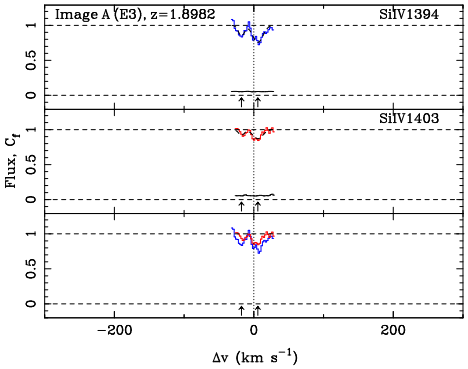
Image A (E3), z=1.8982
SiIV1394
SiIV1403
Flux, C_f
Δv (km s^{-1})

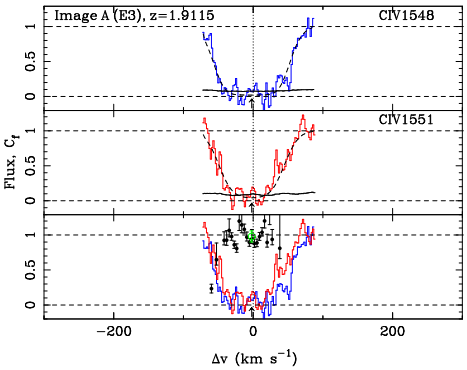
Image A (E3), z=1.9115
CIV1548
CIV1551
Flux, C_f
Δv (km s^{-1})

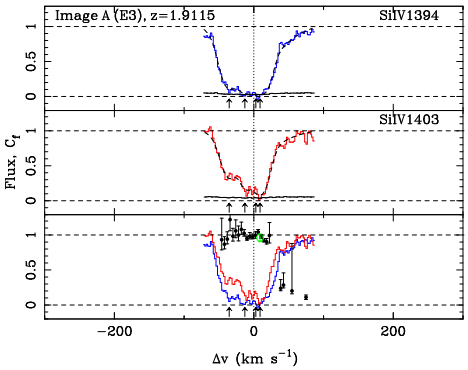
Image A (E3), z=1.9115
SiIV1394
SiIV1403
Flux, C_f
Δv (km s^{-1})

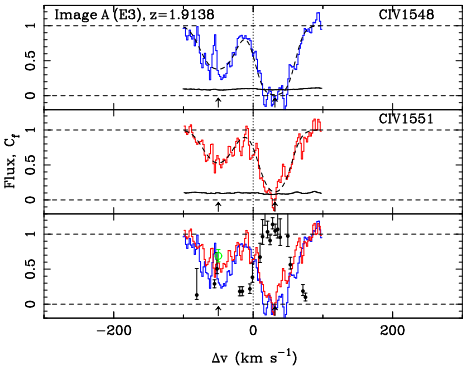
Image A (E3), z=1.9138
CIV1548
CIV1551
Flux, C_f
Δv (km s^{-1})

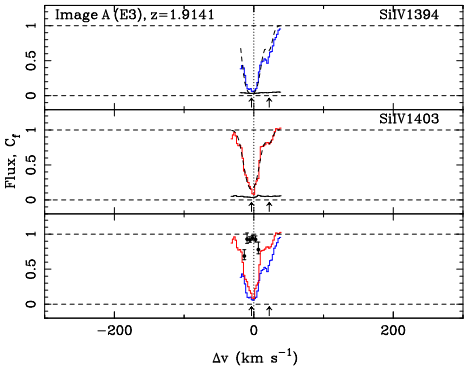
Image A (E3), z=1.9141
SiIV1394
SiIV1403
Flux, C_f
Δv (km s^{-1})

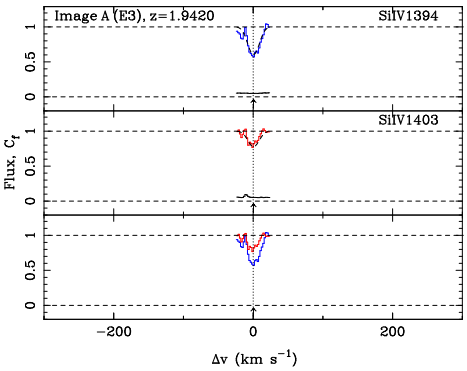
Image A (E3), z=1.9420
SiIV1394
SiIV1403
Flux, C_f
Δv (km s^{-1})

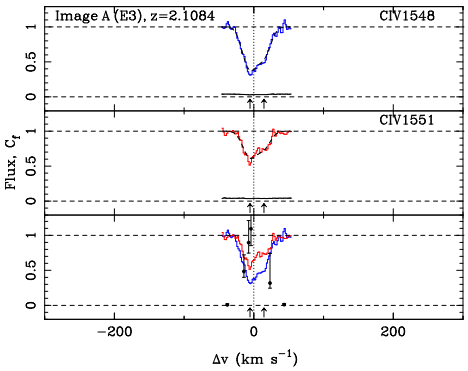
Image A (E3), z=2.1084
CIV1548
CIV1551
Flux, C_f
Δv (km s^{-1})

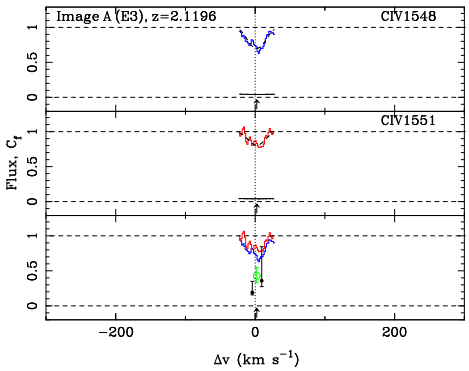
Image A (E3), z=2.1196
CIV1548
CIV1551
Flux, C_f
Δv (km s^{-1})

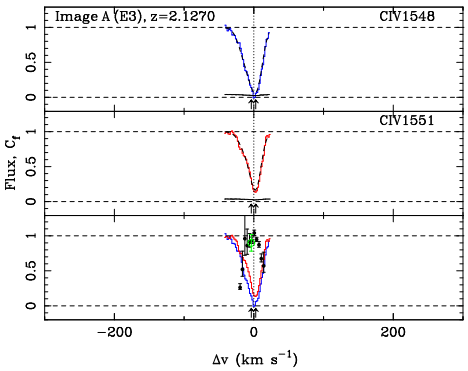
Image A (E3), z=2.1270
CIV1548
CIV1551
Flux, C_f
Δv (km s^{-1})

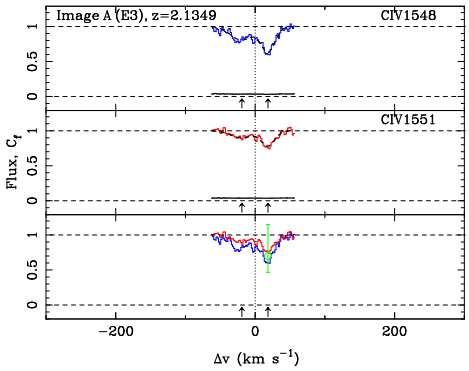
Image A (E3), z=2.1349
CIV1548
CIV1551
Flux, C_f
Δv (km s^{-1})

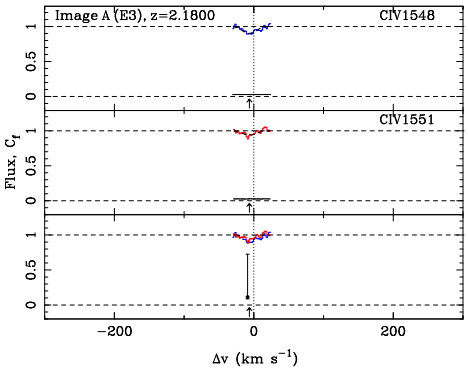
Image A (E3), z=2.1800
CIV1548
CIV1551
Flux, C_f
Δv (km s^{-1})

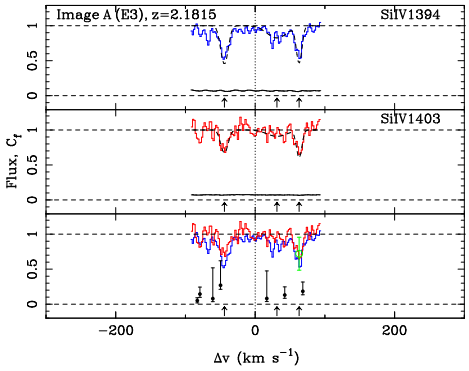
Image A (E3), z=2.1815
SiIV1394
SiIV1403
Flux, C_f
Δv (km s^{-1})

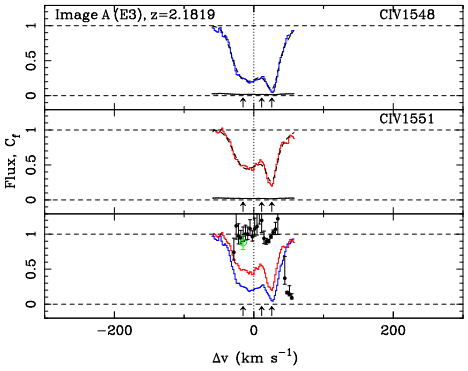
Image A (E3), z=2.1819
CIV1548
CIV1551
Flux, C_f
Δv (km s^{-1})

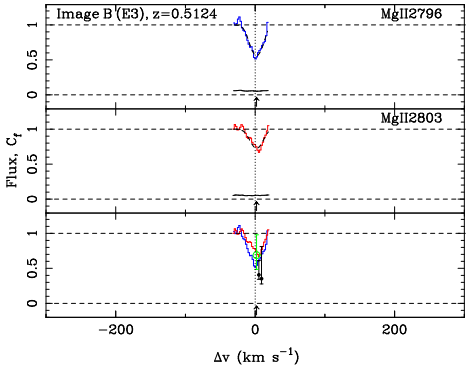
Image B (E3), z=0.5124
MgII2796
MgII2803
Flux, C_f
Δv (km s^{-1})

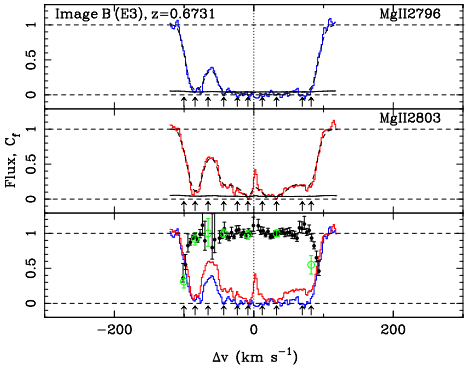
Image B (E3), z=0.6731
MgII2796
MgII2803
Flux, C_f
Δv (km s^{-1})

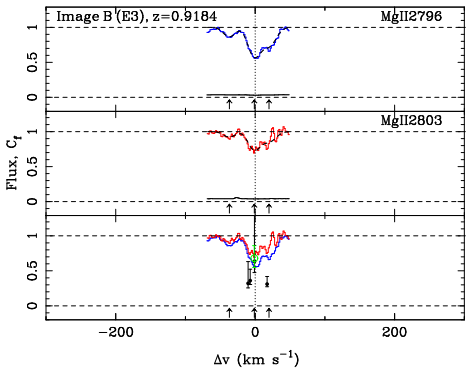
Image B'(E3), z=0.9184
MgII2796
MgII2803
Flux, C_f
Δv (km s^{-1})

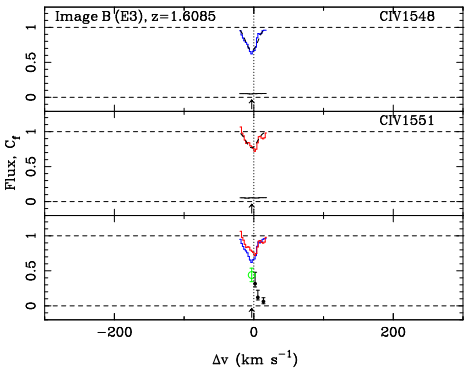
Image B'(E3), z=1.6085
CIV1548
CIV1551
Flux, C_f
Δv (km s^{-1})

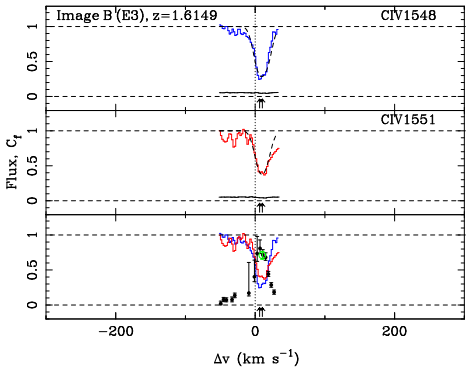
Image B'(E3), z=1.6149
CIV1548
CIV1551
Flux, C_f
Δv (km s^{-1})

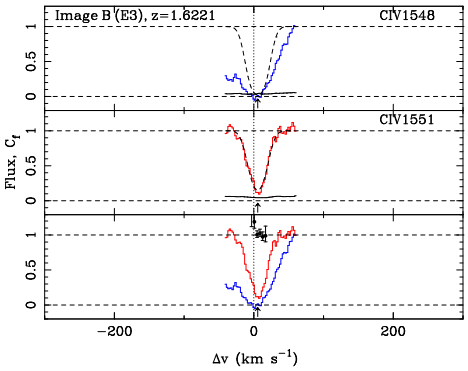
Image B'(E3), z=1.6221
CIV1548
CIV1551
Flux, C_f
Δv (km s^{-1})

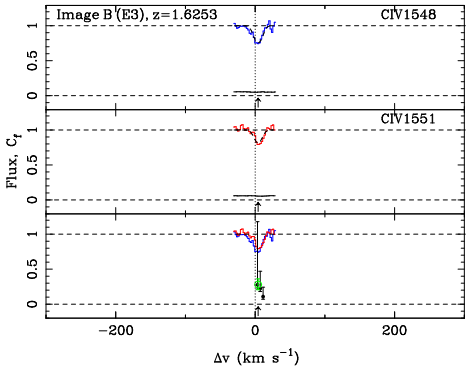
Image B'(E3), z=1.6253
CIV1548
CIV1551
Flux, C_f
Δv (km s^{-1})

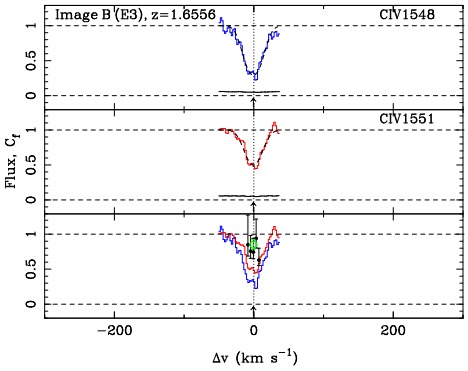
Image B'(E3), z=1.6556
CIV1548
CIV1551
Flux, C_f
Δv (km s^{-1})

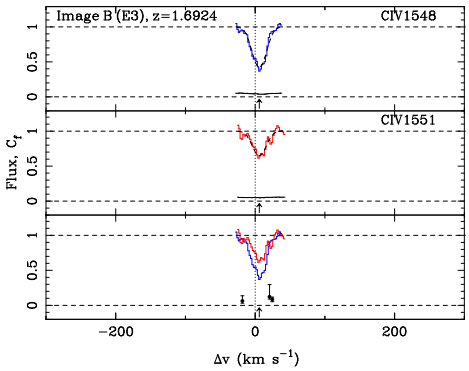
Image B'(E3), z=1.6924
CIV1548
CIV1551
Flux, C_f
Δv (km s^{-1})

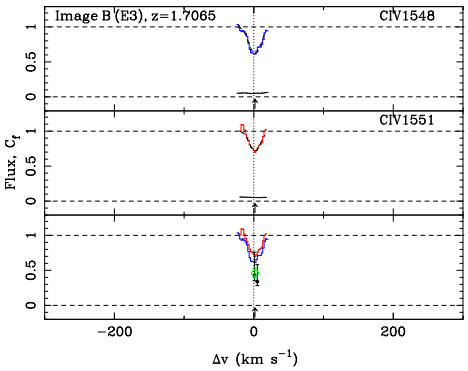
Image B'(E3), z=1.7065
CIV1548
CIV1551
Flux, C_f
Δv (km s^{-1})

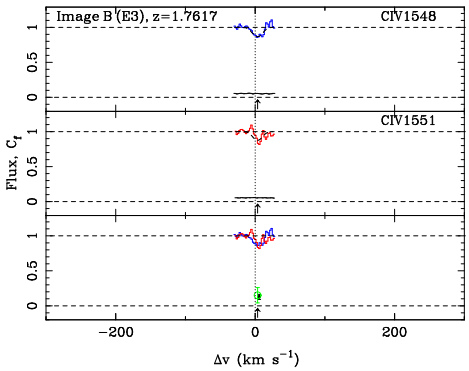
Image B'(E3), z=1.7617
CIV1548
CIV1551
Flux, C_f
Δv (km s^{-1})

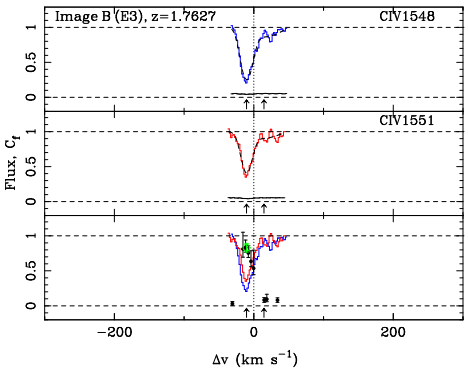
Image B'(E3), z=1.7627
CIV1548
CIV1551
Flux, C_f
Δv (km s^{-1})

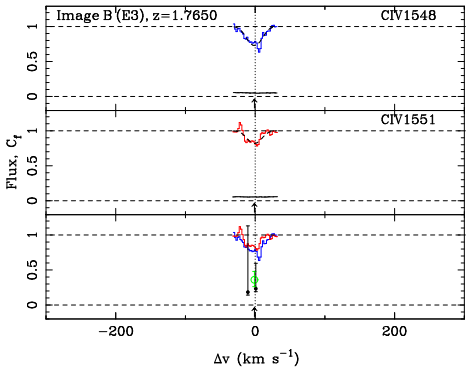
Image B'(E3), z=1.7650
CIV1548
CIV1551
Flux, C_f
Δv (km s^{-1})

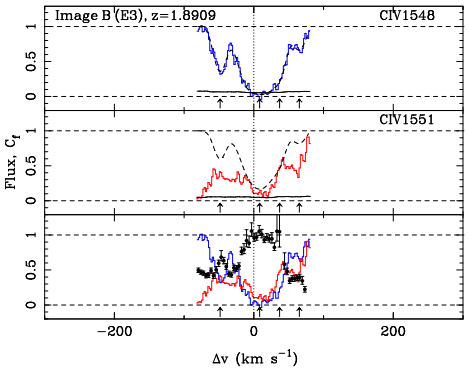
Image B'(E3), z=1.8909
CIV1548
CIV1551
Flux, C_f
Δv (km s^{-1})

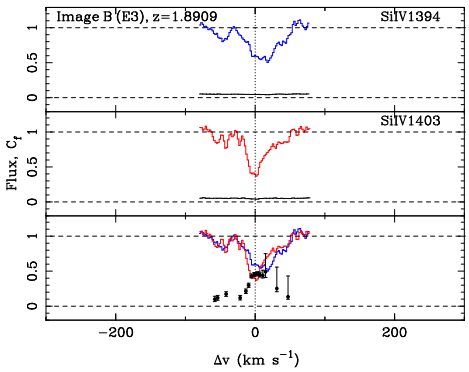
Image B'(E3), z=1.8909
SiIV1394
SiIV1403
Flux, C_f
Δv (km s^{-1})

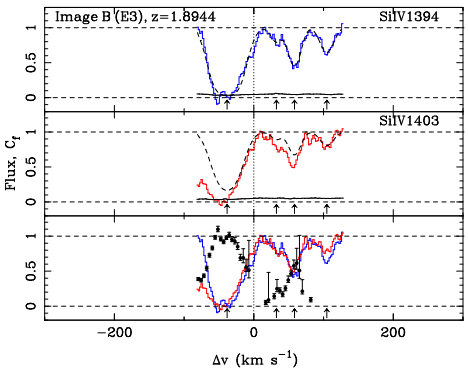
Image B'(E3), z=1.8944
SiIV1394
SiIV1403
Flux, C_f
Δv (km s^{-1})

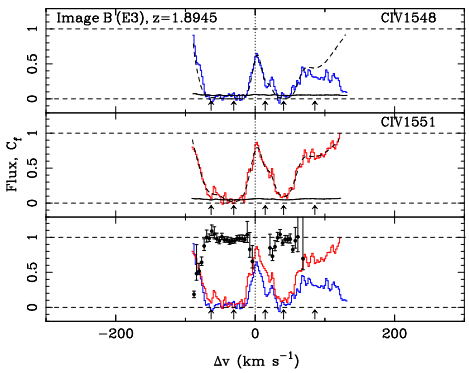
Image B'(E3), z=1.8945
CIV1548
CIV1551
Flux, C_f
Δv (km s^{-1})

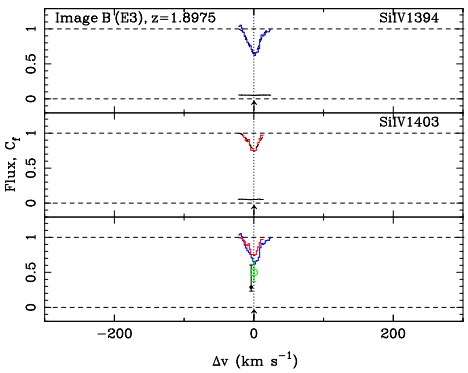
Image B'(E3), z=1.8975
SiIV1394
SiIV1403
Flux, C_f
Δv (km s^{-1})

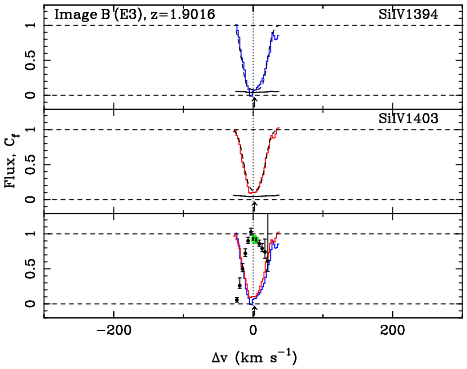
Image B'(E3), z=1.9016
SiIV1394
SiIV1403
Flux, C_f
Δv (km s^{-1})

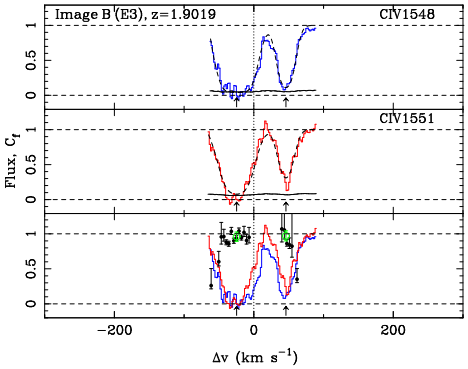
Image B'(E3), z=1.9019
CIV1548
CIV1551
Flux, C_f
Δv (km s^{-1})

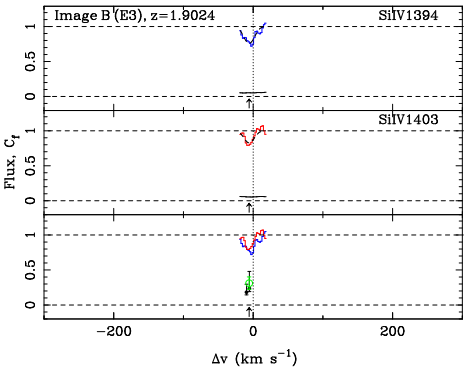
Image B'(E3), z=1.9024
SiIV1394
SiIV1403
Flux, C_f
Δv (km s^{-1})

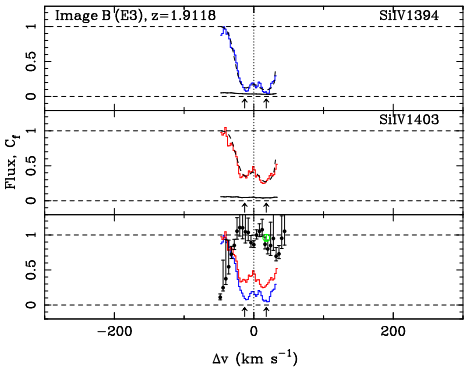
Image B'(E3), z=1.9118
SiIV1394
SiIV1403
Flux, C_f
Δv (km s^{-1})

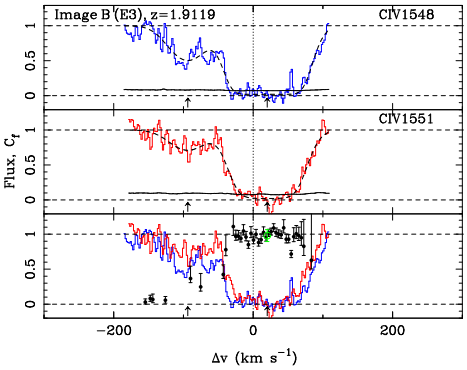
Image B'(E3), z=1.9119
CIV1548
CIV1551
Flux, C_f
Δv (km s^{-1})

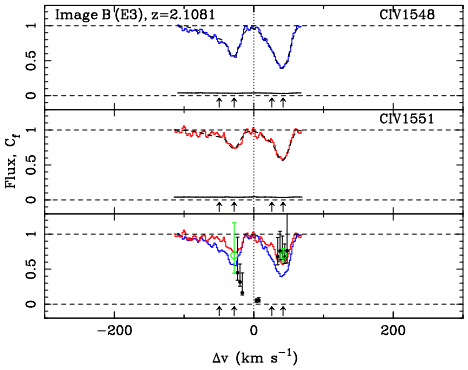
Image B'(E3), z=2.1081
CIV1548
CIV1551
Flux, C_f
Δv (km s^{-1})

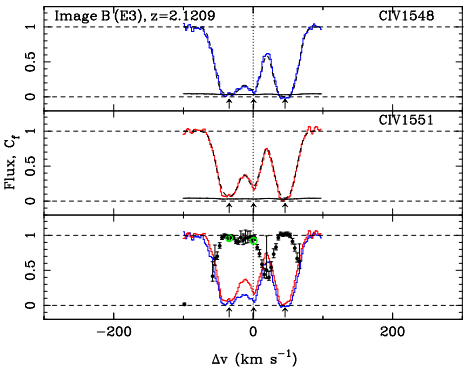
Image B'(E3), z=2.1209
CIV1548
CIV1551
Flux, C_f
Δv (km s^{-1})

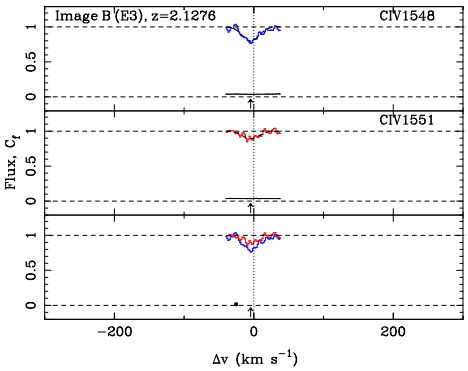
Image B'(E3), z=2.1276
CIV1548
CIV1551
Flux, C_f
Δv (km s^{-1})

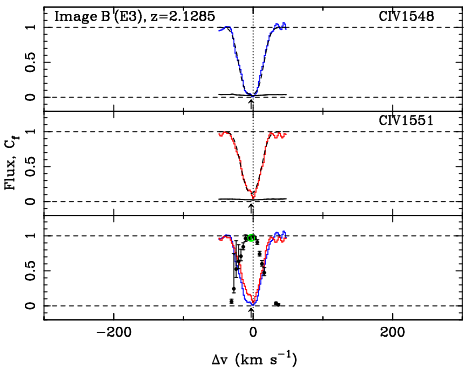
Image B'(E3), z=2.1285
CIV1548
CIV1551
Flux, C_f
Δv (km s^{-1})

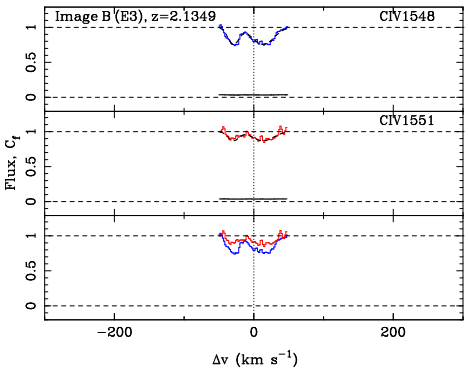
Image B'(E3), z=2.1349
CIV1548
CIV1551
Flux, C_f
Δv (km s^{-1})

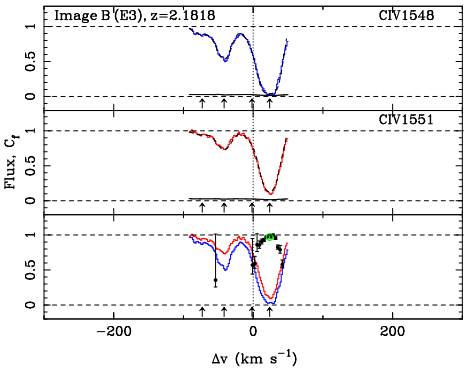
Image B'(E3), z=2.1818
CIV1548
CIV1551
Flux, C_f
Δv (km s^{-1})

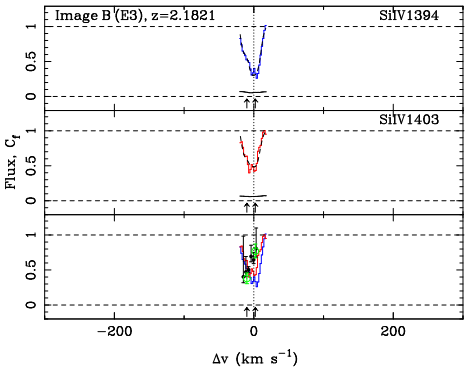
Image B'(E3), z=2.1821
SiIV1394
SiIV1403
Flux, C_f
Δv (km s^{-1})

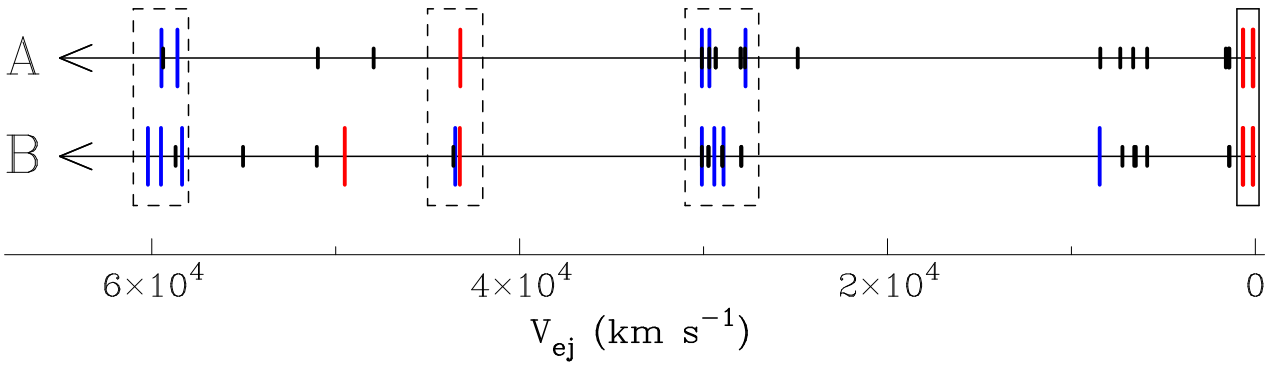

FIG. 4.— Ejection velocity distribution of class-A (red line), B (blue line), and C (black line) NALs and PALs along the sightlines to the images A and B. All Mg II NALs are located outside of the range of the velocity plot. Each of the red lines at $v_{\rm ej} \sim 0$ km s^{-1} surrounded by a solid rectangle includes both C IV and N V PALs, respectively. Three clustering regions are surrounded by dotted rectangles.

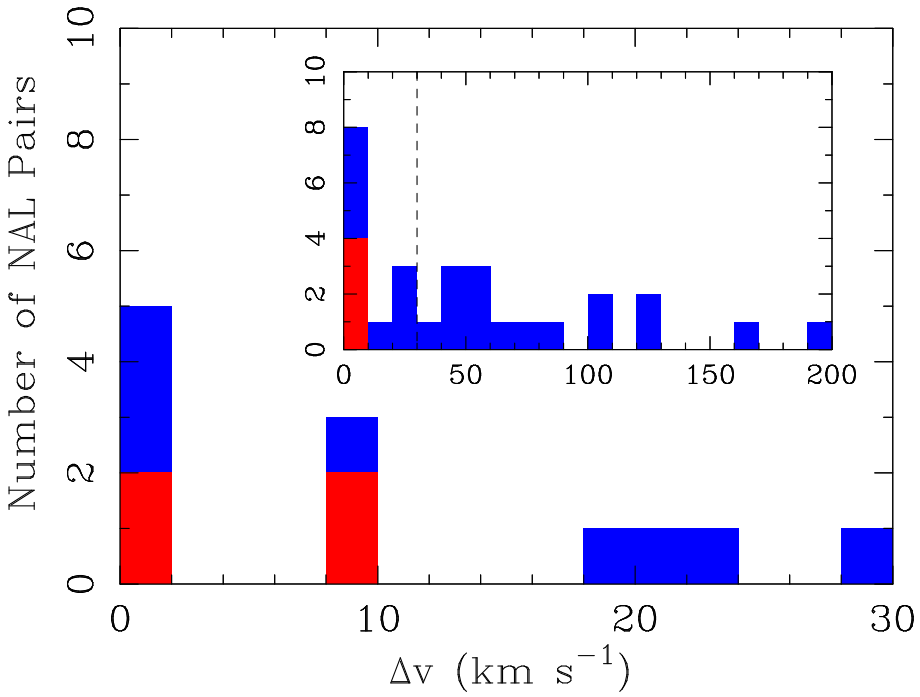

FIG. 5.— Distribution of velocity offset (Δv) between PALs (red histogram) and class-A/B NALs (blue histogram) in the two different images (image A and B) that match each other within $\Delta v \leq 200$ km s^{-1}, as discussed in Section 4.1.4.

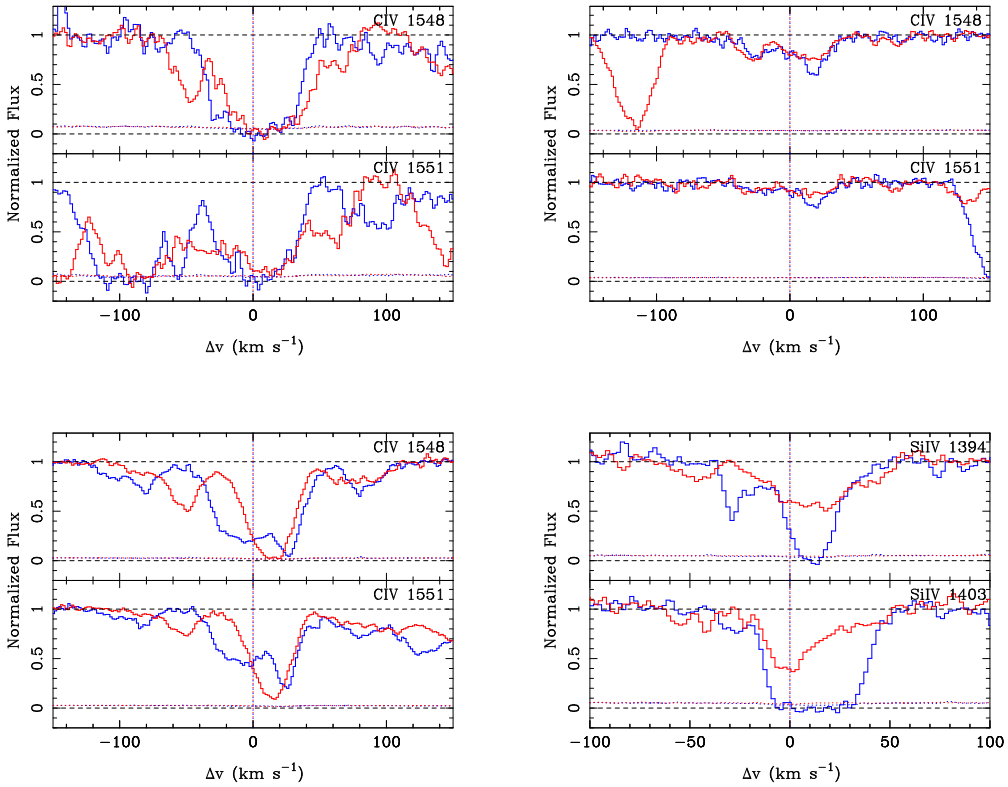

FIG. 6.— Comparison of spectra and their 1σ errors around C IV NALs at $z_{\rm abs} \sim 1.8909$ (upper left), 2.1349 (upper right), 2.1819 (lower left) and Si IV NAL at $z_{\rm abs} \sim 1.8909$ (lower right) in image A (blue histogram) and B (red histogram) spectra for systems that have a small relative velocity between the images.

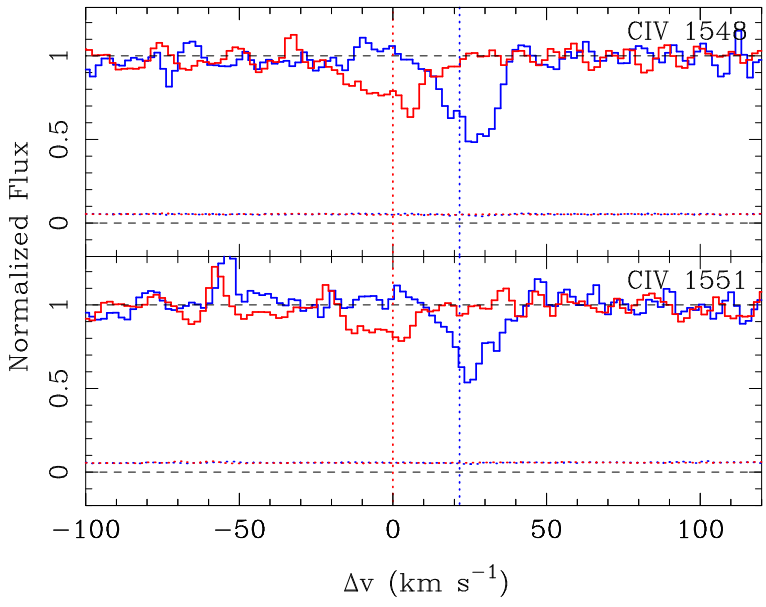

FIG. 7.— Same as Figure 6 but for class-A C IV NALs at $z_{\rm abs} \sim 1.7652$ in image A (blue histogram) and at $z_{\rm abs} \sim 1.7650$ in image B (red histogram). The latter corresponds to the system center ($\Delta v = 0$ km s^{-1}) in this plot.

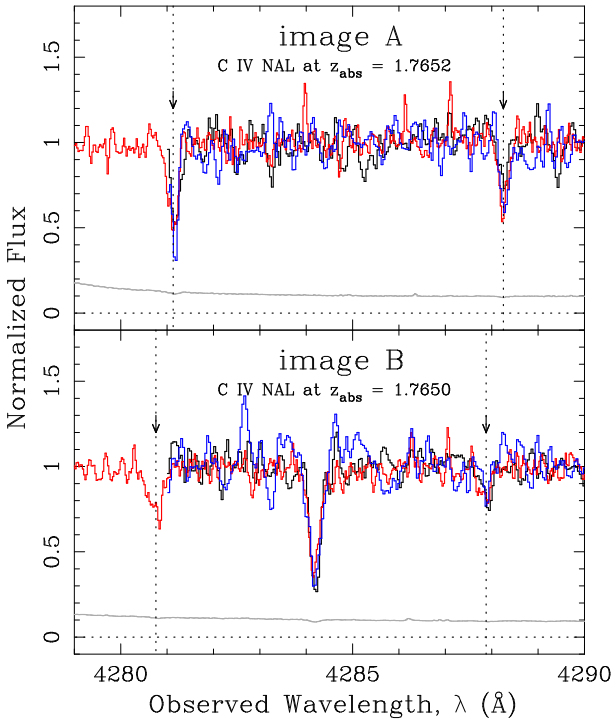

FIG. 8.— Comparison of C IV NALs at $z_{\rm abs} = 1.7652$ in image A (top panel) and at $z_{\rm abs} = 1.7650$ in image B (bottom panel). Black, red, and blue histograms denote spectra in epoch E1, E2, and E3, respectively. The positions of blue and red member of the doublet are marked with down arrows and vertical dashed lines. A strong feature at $\lambda \sim 4284$ Å in the bottom panel is C IV 1551 at $z_{\rm abs} = 1.7627$. Regions at $\lambda \leq 4281$ Å are not covered by the Subaru/HDS spectra in epochs E1 and E3 because they are located at the edge of the CCD.

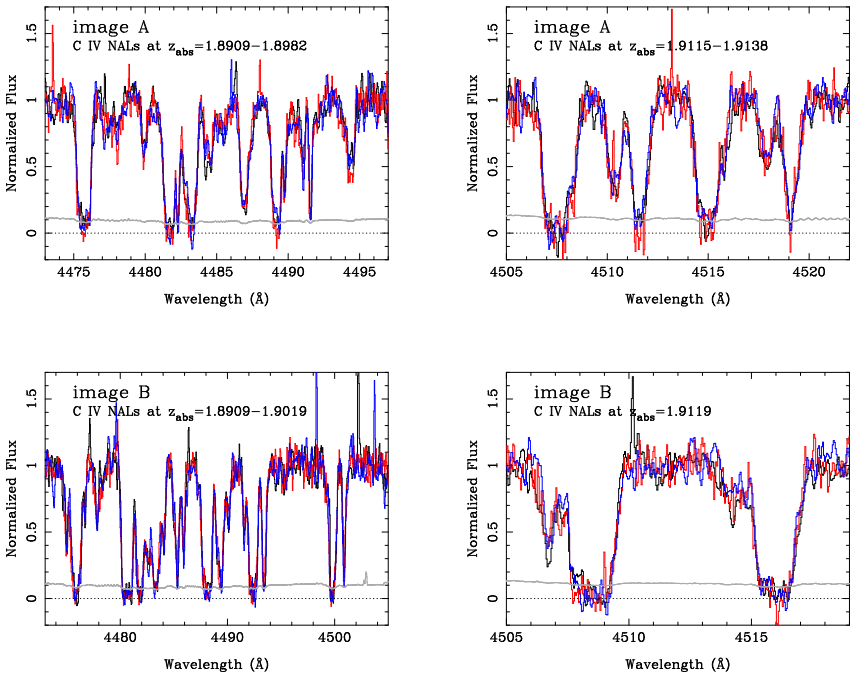

FIG. 9.— Comparison of spectra and their averaged 1σ errors around C IV NALs at $z_{\rm abs} \sim 1.8909$–1.8982 in image A (upper left), 1.9115–1.9138 in image A (upper right), 1.8909–1.9019 in image B (lower left) and 1.9119 in image B (lower right) taken in epoch E1 (black histogram), E2 (red histogram), and E3 (blue histogram).

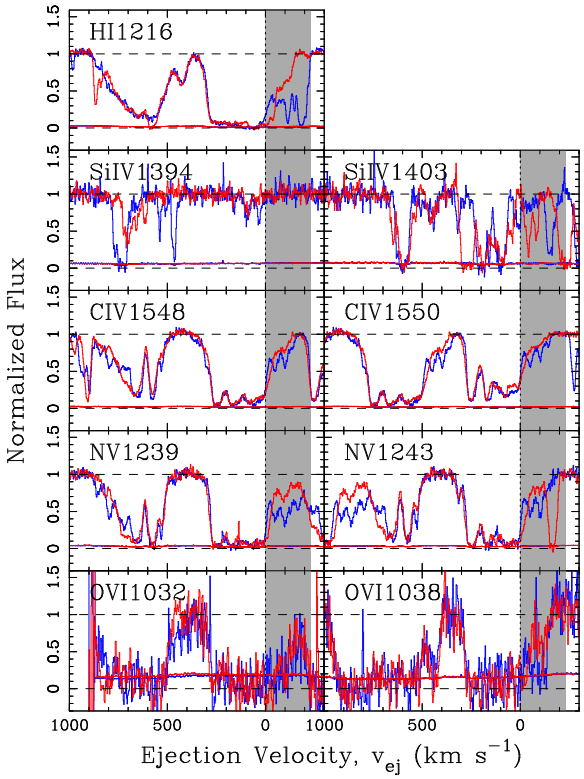

FIG. 10.— Comparison of normalized spectra around Lyα, Si IV, C IV, N V, and O VI PALs detected in the images A (blue) and B (red). The horizontal axis is the offset velocity from the quasar emission redshift, and the vertical axis is the normalized flux. The histograms above the zero flux line are 1σ flux errors. Due to heavy blending with other lines at lower redshift the existence of the Si IV doublet may not be present. The O VI 1032 locate at the edge of the observed spectrum. Absorption features at $v_{\rm ej} < 0$ km s^{-1} in the shaded areas are narrow PALs, while the other features at $v_{\rm ej} > 0$ km s^{-1} are broad PALs.

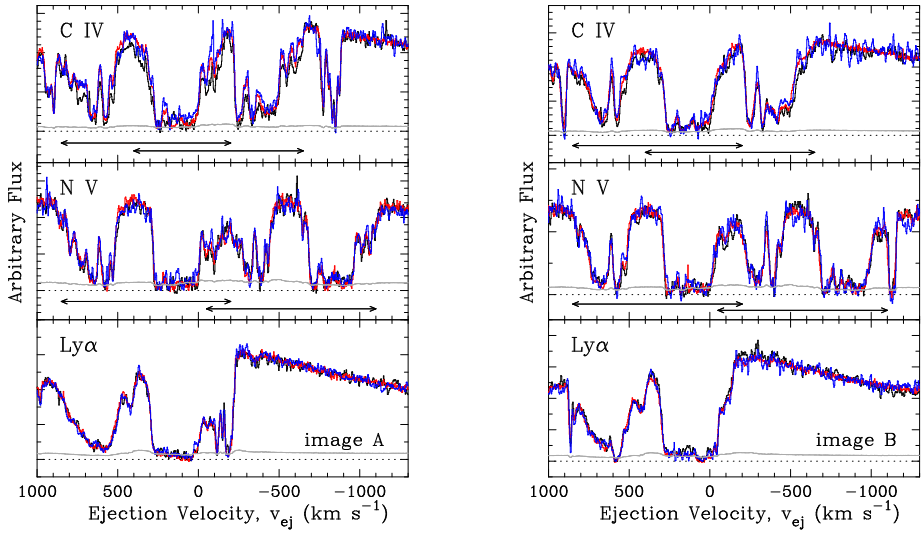

FIG. 11.— Comparison of C IV, N V, and Lyα PALs at $z_{\rm abs} \sim z_{\rm em}$ in images A and B, taken in epochs E1 (black), E2 (red), and E3 (blue). These spectra are scaled to each other by applying a least-square method for unabsorbed wavelength regions at both sides of the PALs. The vertical axis denotes an arbitrary flux because we did not perform absolute flux calibration without flux standard stars. The gray histograms above the zero flux line are 1σ flux error after taking averages of those in three observing epochs. Double-headed arrows in the bottom of the first two panels mark the velocity ranges of the blue and red members of the C IV and N V doublets.

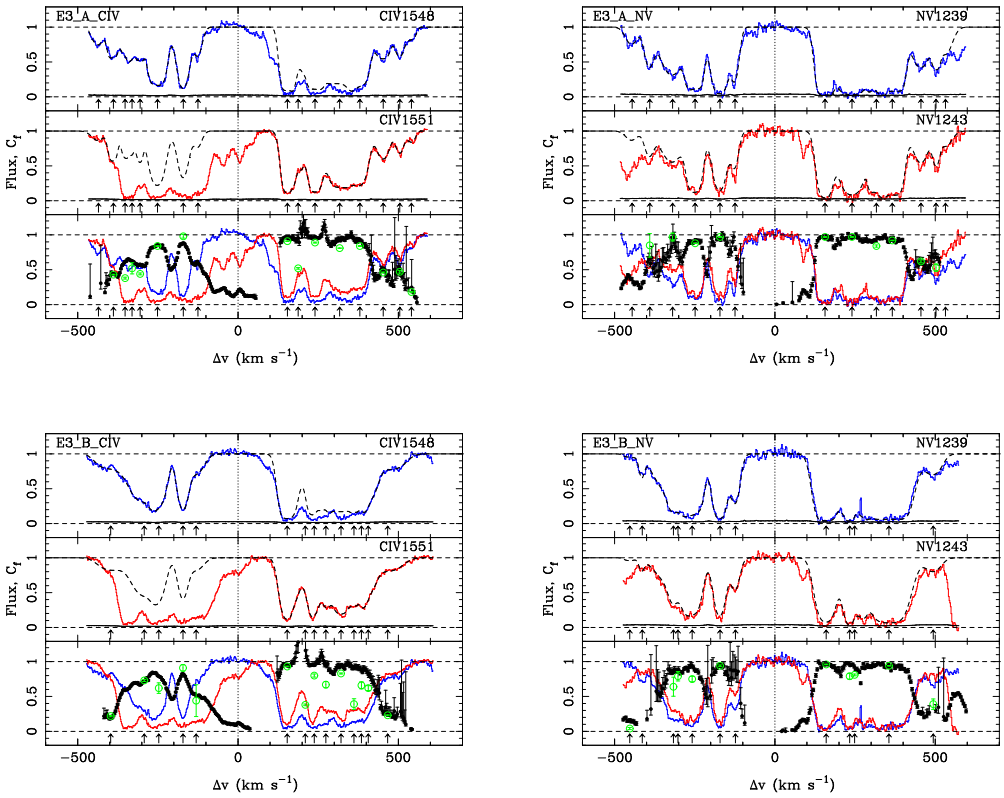

FIG. 12.— Same figures as Figure 3, but for C IV and N V PALs at $z_{\rm abs} \sim z_{\rm em}$. We adopt $z = 2.1927$ as a system center only for the purpose of displaying these velocity plots. Because C IV PALs are self-blended, we fit the profiles of the blue and red members of the doublet simultaneously by multiplying the contributions from them (Misawa et al. 2007b). Spectral regions in the top two panels, for which the profiles of the blue and red members of a doublet (blue and red histograms) and the model profile (dashed line) do not match, suffer from self-blending.

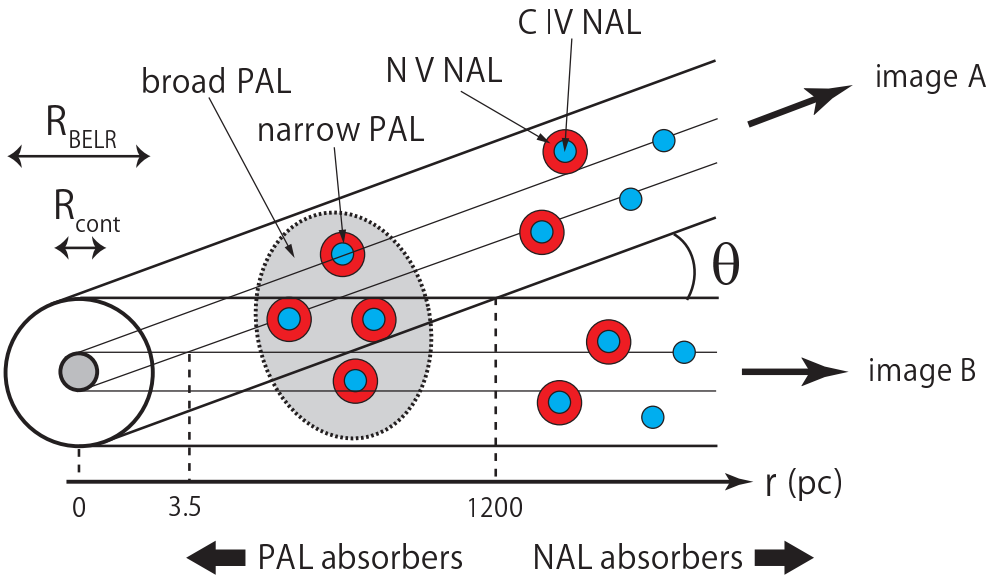

FIG. 13.— Possible geometry of the outflowing wind along our two sightlines toward the lensed quasar SDSS J1029+2623, based on our observations in three epochs. The gray filled circle corresponds to the broad PAL absorber with the minimum acceptable size, while blue and red filled circles are C IV and N V absorbing regions in clumpy clouds as candidates for narrow PAL absorber and intrinsic NALs. The boundary radius of the continuum source (3.5 pc) and BELR (1200 pc) are marked with dashed lines. The NAL absorber's distance is not necessarily larger than 1200 pc, although it is at least larger than the distance of the PAL absorbers. We adopt $14\farcs6$ as the separation angle between two sightlines seen from the source, while Misawa et al. (2013, 2014b) used $22\farcs5$ assuming it is very similar to that seen from us. See Section 5.3 for details.